

**Bimodal radiofrequency pulse distribution of intracloud-lightning
signals recorded by the FORTE satellite**

Abram R. Jacobson (corresponding author)
and
Tracy E. L. Light

Space and Atmospheric Sciences Group
Mail Stop D466
Los Alamos National Laboratory
Los Alamos, New Mexico 87545 USA
tel (505)667-9656 fax (505)665-7395
ajacobson@lanl.gov

This document is being submitted to the American Geophysical Union's Journal of Geophysical Research for possible publication. If the document is ultimately published by JGR, copyright will pass to the AGU. Until its formal publication in a peer-reviewed journal, this document may not be formally cited, and this document is being made available for informal technical communication and discussion only. All formal citation of this document must await its publication in final form in a peer-reviewed journal.

Los Alamos National Laboratory report # LA-UR-02-3236

Abstract

The FORTE satellite's radio-frequency-receiver payload has performed extensive recordings of electromagnetic emissions of lightning discharges. The most commonly occurring such emission arises from intracloud electrical breakdown and is usually recognizable by a pulse followed by a delayed echo from the ground reflection. We have subjected a large cohort of such FORTE-recorded intracloud pulses to exhaustive statistical analysis, which clearly reveals two distinct and highly complementary types of intracloud-discharge pulses. One type of intracloud discharge signal seen regularly by FORTE is associated with discrete and repetitive steps, inferred to be part of a progressive process of stepped-leader breakdown. These pulses (a) are among the weaker radiofrequency signals observable by FORTE, (b) are usually determined to be linearly polarized (when the polarization can be determined at all in the presence of noise), (c) are accompanied by similar neighbors before and after, within several-hundred μs to half a second, (d) exhibit very little random intrapulse fading (amplitude variations within the pulse envelope), and (e) are remarkably narrow ($\sim 0.1 \mu\text{s}$) in width. The intracloud pulses of the opposite type seen regularly by FORTE (a) are extremely intense, (b) are usually randomly polarized, (c) are either isolated in time, or followed by successor pulses which may include some pulses of the polarized/weak type, (d) exhibit deep and irregular fading within the pulse envelope, and (e) have $\sim 1\text{-}\mu\text{s}$ risetimes but several- μs pulse durations, usually with slowly-decaying tails. Comparison of the FORTE recordings of the intense/unpolarized pulses with contemporaneous observations by a ground-based lightning-detection array reveals that their underlying emission process is associated with the "Narrow Bipolar Events" identified by other researchers.

1. Introduction and background

Space-based monitoring and mapping of lightning has recently enjoyed substantial progress due to two extremely successful optical imagers, the Optical Transient Detector, or OTD [Boccippio *et al.*, 2000a], and the Lightning Imaging Sensor, or LIS [Christian *et al.*, 1999]. Progress has also been made on defining the utility of broader types of lightning observations in general, as a proxy for deep tropospheric convection [Boccippio *et al.*, 2000b; Petersen and Rutledge, 1998; Zipser, 1994; Zipser and Lutz, 1994], as a real-time indicator of the imminent severe weather [Williams, 2001; Williams *et al.*, 1989], and as a data constraint on meteorological simulations [Chang *et al.*, 2001].

Compared to optical imagery, reception of radio-frequency (RF) emissions from lightning processes offers a somewhat less direct, but complementary means of remotely sensing lightning from space [Holden *et al.*, 1995; Jacobson *et al.*, 2000; Jacobson *et al.*, 1999; Massey and Holden, 1995; Massey *et al.*, 1998a]. This remote-sensing capability might eventually allow existing RF receivers on satellite constellations to perform real-time tracking of the deep tropospheric convection with which lightning is associated in certain well-characterized and important weather regimes [Boccippio *et al.*, 2000b; Petersen and Rutledge, 1998; Zipser, 1994; Zipser and Lutz, 1994]. The location of the lightning could be determined via RF measurements simultaneously from a constellation of sensors performing time-difference-of-arrival (TDOA) signal processing. Potential benefits of this approach include retrieval of the height of the lightning emission, which is an indicator of the vigor of the convective system and which is thought to be a predictor of the likelihood of severe weather [Williams, 2001]. Another potential benefit of RF lightning records is identification, from the RF waveform, of the specific lightning process, e.g. return stroke, intracloud leader, etc. At present we do not adequately understand how to infer convective-storm characteristics from radio-frequency signals collected in space. Reaching such an understanding requires detailed and systematic study of large collections of RF signals recorded under the observational constraints of a space-borne sensor. This can be done with single research satellites, albeit without the location capabilities of constellation TDOA. Here we present several statistically-based distinguishing characteristics of the two main RF emissions from intracloud lightning processes observable from space, based on data from the FORTE research satellite. These characteristics provide a means of distinguishing lightning processes based on details of recorded RF lightning signals.

The most established approach to real-time monitoring of lightning is via ground-based arrays of electromagnetic sensors. These are principally arrays of low-frequency (LF; 30-300 kHz) and very-low-frequency (VLF; 3-30 kHz) electric (and in some cases magnetic)

sensors with TDOA geolocation of the radiating strokes responsible for the detected LF/VLF signal. The most established such system is the National Lightning Detection Network (NLDN) in the United States [Cummins *et al.*, 1998], and there are several others worldwide. The electromagnetic signals seen from such arrays in the radiation far field are horizontally-propagating (Earth-skimming, or at longer range ducted in the Earth-ionosphere waveguide) LF/VLF radiation from vertical currents known as “sferics”.

By contrast, the very-high-frequency (VHF; 30-300 MHz) radiation detected by radio-frequency receivers is normally generated by the air-breakdown processes which often, though not always, are associated with detectable sferics [Proctor, 1981; Proctor *et al.*, 1988; Rhodes *et al.*, 1994; Shao *et al.*, 1999; Shao and Krehbiel, 1996; Shao *et al.*, 1995; Taylor, 1978; Taylor *et al.*, 1984]. Thus, the lightning signatures gathered by ground-based LF/VLF arrays on the one hand, and by VHF receivers, on the other hand, must be expected *a priori* to be related to complementary aspects of the complex lightning process. Moreover, the VHF signals observed from lightning are more likely to accompany intracloud (IC) processes than to accompany strokes to ground [Jacobson *et al.*, 2000].

From space, a VHF receiver is exposed to the cumulative radio noise, most of it anthropogenic, deriving from a large area of the Earth. For example, the FORTE satellite at altitudes near or exceeding 800 km is exposed to noise from a disk on Earth of diameter several-thousand kilometers [Jacobson *et al.*, 1999]. Except over a very few radio-quiet areas of Earth, FORTE is thus exposed to myriad communication, industrial, and radar signals within the operating passband. This tends to disfavor the reception and recognition of weak signals caused by lightning, which might otherwise be straightforward to receive and to recognize using a ground-based VHF system that is less exposed to sources of noise. The satellite-based receiver system is *a fortiori* biased toward the most intense VHF emissions from lightning processes.

The FORTE satellite [Jacobson *et al.*, 1999] was launched in 1997 into a circular, 800-km altitude orbit inclined 70° from the equatorial plane. FORTE has been used continually since launch to observe signals of lightning with both RF [Jacobson *et al.*, 2000; Jacobson *et al.*, 1999; Jacobson and Shao, 2002a; Jacobson and Shao, 2002b; Light and Jacobson, 2002; Shao and Jacobson, 2002; Tierney *et al.*, 2001; Tierney *et al.*, 2002] and optical sensors [Kirkland *et al.*, 2001; Light *et al.*, 2001; Suszcynsky *et al.*, 2000a]. FORTE has been useful in gathering signals of strong lightning events from most regions of the world where thunderstorms occur.

One of the first and most basic of FORTE's findings was that RF "transionospheric pulse pairs", or TIPPs, observed earlier with Blackbeard [Holden *et al.*, 1995; Massey and Holden, 1995; Massey *et al.*, 1998a] are simply the manifestation of a time-delayed ground-reflection following the initial RF pulse from an intracloud lightning discharge [Jacobson *et al.*, 1999]. The second pulse can complicate the signal interpretation, but correspondingly, can provide more information. For example, during a flash, the relative pulse-pairs' interpulse separations are proportional to the height of emission above the RF-reflective ground. Thus, the ratio of heights of the various pulses within the flash can be inferred [Jacobson *et al.*, 1999], even if the lightning horizontal location is not known. Second, for lightning whose horizontal location is known, even approximately, the interpulse separations can be used to infer the *absolute emission heights*, not just ratios between emission heights [Jacobson *et al.*, 2000].

Beyond the exploitation of viewing geometry to infer the emission height of IC radio emissions, Light and Jacobson [2002] have more recently examined the characteristics of these pulses and the incidence of accompanying optical signals observable by FORTE's photodiode detector (PDD) [Kirkland *et al.*, 2001]. A surprising result was found: Above a certain threshold amplitude, RF pulses occurring at cloud height become *less likely to be accompanied by an optical signal, as the RF pulse amplitude is further increased* [Light and Jacobson, 2002, note their Figure 11]. In other words, for this variety of IC discharge, *as the RF becomes more observable from space, the accompanying optical pulse becomes less observable from space*. Moreover, the RF pulse intensity (measured as electric field squared, or E^2 , in units of $(\text{v/m})^2$) at the satellite, sufficed by itself to predict the likelihood of an accompanying optical pulse: At the threshold value $E^2 \sim 2 \times 10^{-7} (\text{v/m})^2$ in a 22-MHz passband centered at 38 MHz, the probability of an accompanying optical signal is maximum, and as E^2 is further increased, that probability then monotonically decreases, out to the most intense RF pulses seen from IC processes: $E^2 > 10^{-5} (\text{v/m})^2$. These strong RF pulses that are unaccompanied by an observable optical counterpart, we will call "dark IC lightning" for short. While "dark" is most likely an exaggeration, it conveys the practical difficulty of observing the process optically from space.

We point out that if the emission latitude and longitude are known, then it would be more physically meaningful to express this RF-intensity threshold in terms of effective radiated power (ERP) *at the source* in the IC discharge. However, for the majority of RF pulses observed by FORTE, we do not know for sure where the source lies, other than knowing that it must be in the troposphere or lower stratosphere above that part of Earth visible from the satellite. Thus, in order to use the greatest number of data points (to enhance statistics) we must often draw conclusions based on observable parameters at the satellite,

rather than at the source. This was necessitated in comparing the RF and PDD observations, because of the small efficiency of common observations [*Light and Jacobson*, 2002] and the consequent small number of candidate events.

There have been several ground-based observations of exceptionally intense RF pulses emitted by IC processes. LeVine [1980] reported on intense high-frequency (HF; 3-30 MHz) radiation from a certain class of IC discharges. He identified this class as also exhibiting a distinctive LF and medium-frequency (MF; 300 kHz-3 MHz) vertical sferic that was much shorter in total duration (~ 10 μ s or less) than are ordinary sferics from common lighting processes, which have durations on the order of 100 μ s. The sferic of LeVine's study we will call a Narrow Bipolar Event (NBE). He noted that NBEs "appeared to be relatively isolated and infrequent in the data...", relative to more familiar, lower-amplitude emissions.

Willett *et al* [1989] reported on wideband (DC - 50 MHz) measurements of the vertical electric field signatures of NBEs, i.e the NBEs' wideband sferics. They discovered (see e.g. Figure 2 of Willett *et al*) that the intense HF emissions were due to numerous spikey, disorganized and sharp electric-field excursions superimposed on the slower "sferic". (This is in distinct contrast to the relationship of low-frequency and high-frequency outputs from the negative cloud-to-ground stroke over seawater [*Jacobson and Shao*, 2002a; *Krider and Leteinturier*, 1996; *Willett et al.*, 1990; *Willett and Krider*, 2000; *Willett et al.*, 1998], in which the various frequencies' output levels are manifestations of the same pulse structure.) The NBEs of Willett *et al* [1989] could have either sign of their leading electric-field sferic excursion, with positive being upward-directed by convention. The positive and negative NBEs we will call "NPBEs" and "NNBEs" respectively. It was shown that the NBEs' HF spectra were flatter (i.e., whiter) than were the spectra of RF emissions from return strokes, and that above 10 MHz, the NBE RF emissions were increasingly powerful compared to those of return strokes. Therefore it would not be surprising if the RF emissions accompanying NBEs were also the most powerful lightning signals in the VHF also, the range below which satellite observations of RF pulses from lightning are not practical [*Jacobson et al.*, 2000].

The Blackbeard radio receiver developed by W. T. Armstrong [*Holden et al.*, 1995] on the Alexis satellite yielded numerous RF recordings of intense HF/VHF pulses from IC discharges, with echo pulses delayed by 10's of μ s [*Massey and Holden*, 1995; *Massey et al.*, 1998a] from the initial pulses. Indeed, the Blackbeard trigger was sufficiently susceptible to anthropogenic RF noise that the trigger threshold needed to be set high enough that only these intense HF lightning emissions could be recorded. The weaker RF

emissions of lightning were not seen by Blackbeard. Rather, the RF pulses triggered upon by Blackbeard were of an intensity corresponding to the strongest seen by FORTE. A PDD-like optical detector in the Blackbeard payload never succeeded in triggering on accompanying optical pulses. Whether this was due to an operational difficulty, or was a precursor of the recent “dark IC lightning” found with FORTE [Light and Jacobson, 2002], can not be determined. However, the finding is consistent with the Blackbeard RF pulses’ having been from dark IC lightning.

Smith *et al* [1999] reported on the coordinated use of both sferic and HF ground-based measurements and contemporaneous meteorological radar data, which taken together finally began to place NBEs into a micro-meteorological context. The sferic and HF observations used multi-path signal reception at long range, in which the ionospherically reflected signal was detected. The first path was via an ionospheric reflection, and the second path was via both a ground reflection and then an ionospheric reflection. The pulse-separation time between these two signal arrivals could then be used to infer the emission altitude [Smith *et al.*, 1999, see their Figure 2]. It was shown that the observed NBEs occurred in close proximity to the high-radar-reflectivity core of the storm. The emission heights inferred from pulse separations were on the order of 10 km, which was high in the vertical structure of these particular New Mexico air-mass thunderstorms. The emissions also occurred within regions of maximum radar reflectivity for the storm.

The NBE sferics observed with calibrated sensors by Smith *et al* had to be radiated by an extremely large electric-dipole-moment rate of change, around 28 C-km/ms, which is tenfold higher than the corresponding values inferred for more common IC sferic-emitting events known as “K-changes” [Krehbiel, 1981]. It was shown that the implied NBE signal-emission region had to have a size scale on the order of hundreds of meters to a kilometer, in order to be consistent with the HF and sferic data. The NBEs observed by Smith *et al* tended to be isolated, with no accompanying signals occurring within tens of milliseconds of the NBEs. The accompanying HF signals were $\sim 10\ \mu\text{s}$ in duration, with a shorter risetime than falltime [Smith *et al.*, 1999, e.g. their Plate 2].

A further advance in the characterization of NBEs was provided by the lightning-mapping array (LMA) developed by the Langmuir Laboratory at New Mexico Institute of Mining and Technology [Rison *et al.*, 1999; Thomas *et al.*, 2001]. This is a ground-based VHF lightning mapper recording pulses at several separated stations and performing TDOA to determine three-dimensional location of RF emission sources. The LMA was operated in regions covered also by LF/MF sferic-waveform-recording sensors. Rison *et al* [1999] used the sferic waveforms to identify NBEs via their unique narrow pulse, and used the LMA data (a) to locate the accompanying VHF emission, (b) to characterize the

amplitude of the VHF pulse, and (c) to place the NBE event within the context of IC lightning flashes capable of containing other VHF emissions. It was found that *the NBEs tended to occur at the exact initiation of IC flashes*, and that their VHF intensities were orders-of-magnitude stronger than those of the following VHF emissions within the flash. The initiatory NBE in an IC flash also tended to occur somewhat lower in the storm than the following VHF emissions that occurred in the same flash. This was interpreted as the NBE's being located between a negative charge layer (underneath) and a positive charge layer (above), and the following VHF emissions' arising from negative breakdown within the positive-charge layer. Rison *et al* [1999] reconciled the earlier finding [Smith *et al.*, 1999] that NBEs tend to be isolated, with the newer finding that NBEs tend to occur at the exact initiation of IC discharges, by noting that the earlier measurements were done at long range and hence were unlikely to trigger on the weaker follow-on emissions from the leader propagation through the overlying positive charge layer. Thomas *et al* [2001] studied a large number of flashes containing both initiatory NBEs and follow-on emissions. The source ERP (in the LMA passband of 63-69 MHz) was shown to be typically ~1 W for follow-on emissions, but > 100 kW for initiatory events associated with NBE sferics. Another outcome of the LMA work was that although the intense NBE-associated VHF emissions almost always occurred at the start of IC flashes, many (perhaps most) IC flashes did not show such an initiating event. The LMA pulse-capture scheme does not allow the pulsewidth or pulse shape to be readily measured.

2. Basic FORTE observations of IC-discharge signals

2.1 RF payload characteristics

FORTE receives, digitizes, stores, and downlinks discrete records of VHF lightning time series waveforms of the RF electric field, E. The radio-frequency receiver whose data are used in much of this study comprises dual, simultaneous 50-Megasample-per-second passbands that are simultaneously digitized, each analog-filtered to 22-MHz bandwidth. In the data to follow, we always operated the RF payload with at least one of the 22-MHz-bandwidth channels placed in the range 26-48 MHz, with a nominal 38-MHz center ("low band"). During some of the study, the other 22-MHz-bandwidth channel was tuned to "high band" (118-140 MHz), with a nominal 130-MHz center. Otherwise, the other 22-MHz channel was tuned to low band also, so that both channels were on low-band, but on orthogonal antennas. The trigger for both channels was common and was always derived from low band. The performance of the FORTE RF payload, plus some of the initial characteristics of the lightning observations, have been described in detail elsewhere [Jacobson *et al.*, 1999], so only the most pertinent information is repeated here.

A major advance of FORTE over Blackbeard is in the triggering scheme. FORTE uses a multichannel-coincidence trigger that allows triggering on very weak lightning emissions compared to those which could be studied with Blackbeard. There are eight “trigger subbands” in each 22-MHz-wide receiver channel. Each 1-MHz-wide trigger subband has a noise-compensation option, so that the trigger threshold is set either in absolute level or as dB *above a low-pass-filtered noise level* in that 1-MHz subband, i.e. as a “noise-riding threshold”. In this way the trigger system can in practice trigger on lightning signatures that would otherwise be overwhelmed by anthropogenic radio carriers appearing in the overall receiver passband. In the data used here, we use noise-riding-threshold triggering and require five (out of eight) 1-MHz subbands to trigger in approximate coincidence. We typically require the signal to rise at least 14 - 20 dB (depending on the program and the intended class of lightning signals) above the noise background in each 1-MHz subband contributor to the “5-out-of-8” logical-OR condition. These contributing channels must arrive within a coincidence time of 162 μ s of each other. This coincidence window allows for arrival of different frequencies from the same event, in the presence of ionospheric dispersion of the pulse. (“Ionospheric dispersion” is the effect of the ionospheric plasma's imposing a group delay on the rf pulse, with the delay varying roughly as $1/f^2$.) The exceptional performance of the multichannel-coincidence trigger has allowed FORTE to trigger on, and to record, lightning VHF emissions with ERP (in the passband 26-48 MHz) ranging from Blackbeard-like levels ($\sim 10^6$ W) down to very weak levels ($\sim 10^3$ W) [Jacobson *et al.*, 2000].

The ionospheric $1/f^2$ dispersion causes the lowest frequencies to arrive latest, as in a “chirp”. For this reason the VHF signals which have been transmitted through the ionosphere are referred to as “chirped” signals. Similarly, the signal-processing step of removing the dispersion is called “dechirping”. We perform dechirping on all archived VHF signals from FORTE.

Both 22-MHz-bandwidth channels are connected to different linear polarizations of a two-polarization log-periodic antenna. The antenna is mounted on a boom toward the satellite nadir, usually within a few degrees or less of true pointing. The antenna is designed to place an approximate minimum (throughout the VHF spectrum) on the limb of the Earth as seen from FORTE, and a lobe maximum at nadir. The limb is a circle of arc-diameter 6,400 km on the surface of the Earth. The performance of this antenna system is described in detail elsewhere [Jacobson and Shao, 2002b; Massey *et al.*, 1998b; Shao and Jacobson, 2001; Shao and Jacobson, 2002].

The Data Acquisition System (DAS) contains enough memory for up to 0.8 seconds (cumulative) of 12-bit data simultaneously from the two 22-MHz channels. Each record

is triggered (see above) and has adjustable pre/post-trigger ratio for the record-trigger alignment. We typically use 400- μ s records that contain 100 μ s of pretrigger samples and 300 μ s of posttrigger samples.

The DAS is capable of beginning a new record 162 μ s after the end of the previous record, so that FORTE records can effectively be strung-together to form a quasi-continuous registration of VHF signatures arriving one-upon-the-other within a flash. We find in practice that the registration of records is not impeded by the necessary DAS dead time between records, but rather is spaced wider apart by the natural cadence of the emission process itself.

The configuration described above was followed between launch (August 1997) and December 1999. During this ~ 28-month campaign, FORTE gathered over 3-million data records, the vast majority of which were due to VHF emissions from lightning.

2.2 Basic evidence for a bimodal distribution of VHF signals from IC lightning

FORTE VHF pulsed signals having a delayed echo following the initial pulse have been found to be due to IC discharges [Jacobson *et al.*, 1999]. The double-pulse structure of the signal provides a useful indicator of the signal origin's being intracloud, or at least significantly above the ground. It has been shown elsewhere that in only rare circumstances can a discharge at cloud level escape generating a second pulse from ground reflection [Jacobson and Shao, 2002b; Massey *et al.*, 1998a; Tierney *et al.*, 2002]. Signals that do not have an echo must *a fortiori* be generated near the ground. How near the ground varies with elevation angle of the satellite (from the signal source), but typically any signal source more than 1 km above the ground can be easily distinguished from a signal source exactly on the ground. The foremost example of a signal source *on the ground* is the VHF transient accompanying the initiation of negative cloud-to-ground strokes [Jacobson and Shao, 2002a]. The remainder of this paper will be concerned exclusively with intracloud pulse emissions, having a telltale ground-reflection echo.

Figure 1 shows spectrograms of typical but contrasting VHF pulses from intracloud lightning. In addition to lightning in these signals, there is some interference (horizontal bands) from anthropogenic radio carrier transmissions ("carriers"). In each spectrogram, the ground-reflection echo is delayed ~50 μ s from the primary pulse. This implies that the echo has propagated ~50 μ s/c ~17 km further than the primary pulse. If the satellite were at zenith relative to the lightning, this would imply a height above ground of ~8.5 km. This height is a lower estimate; if the satellite is not at zenith, the implied RF-emission height must be greater [Jacobson *et al.*, 1999]. Each signal exhibits obvious

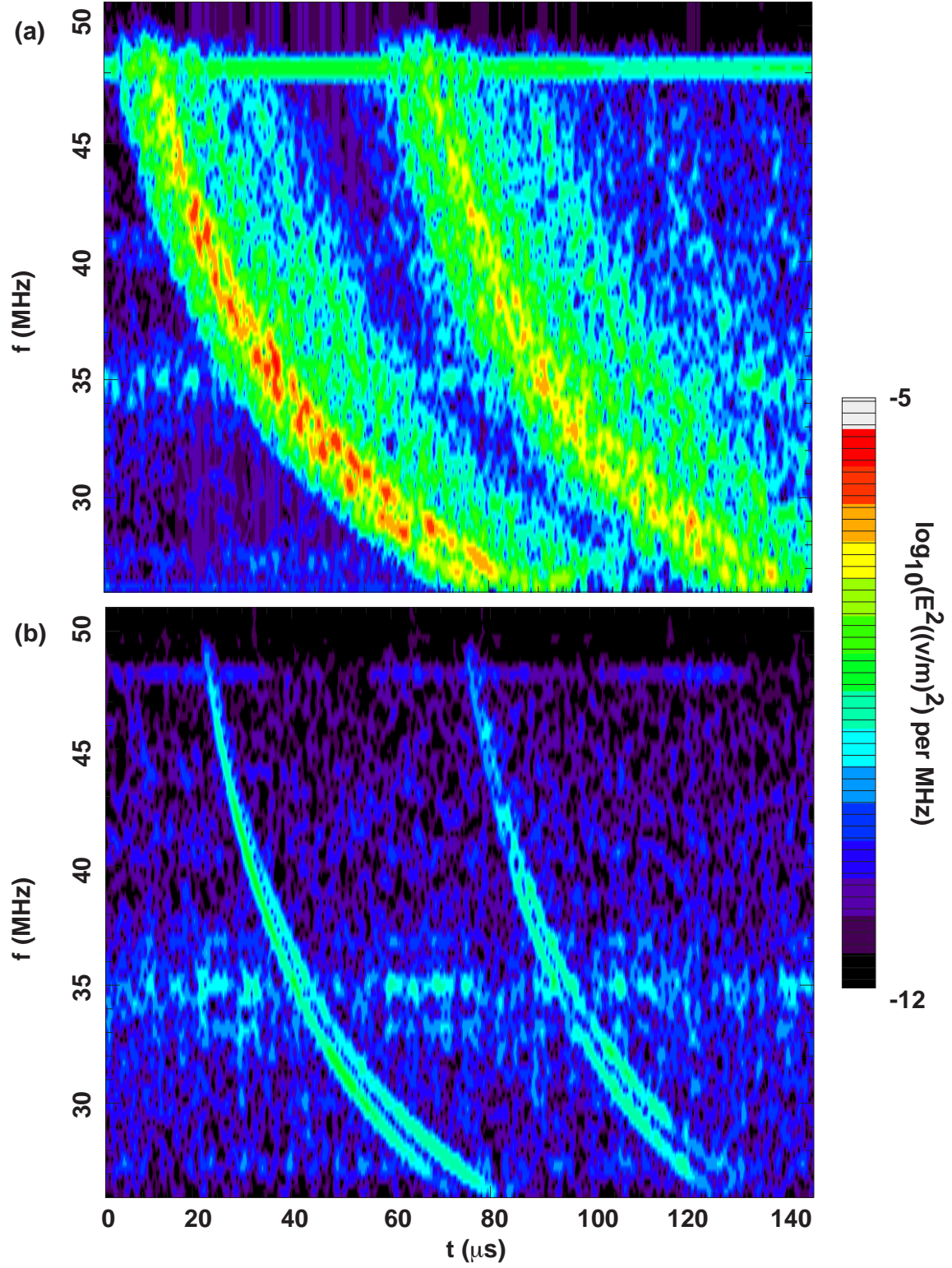


Figure 1: Spectrograms of (a) strong intracloud pulse, and (b) polarized/coherent intracloud pulse. The ground echo is seen at a delay of $\sim 50 \mu\text{s}$ relative to the main pulse.

spectral dispersion from ionospheric propagation [*Jacobson et al.*, 1999; *Roussel-Dupré et al.*, 2001], with most of the group delay due varying as $\sim \text{TEC}/f^2$, where TEC is total electron content, that is, the path integral of the electron density along the propagation path, and where f is the radio frequency. (The TEC is inferred to be $5.36 \times 10^{17} \text{ m}^{-2}$ in Figure 1a and $3.43 \times 10^{17} \text{ m}^{-2}$ in Figure 1b, using the automatic data reduction described elsewhere [*Jacobson et al.*, 1999]).

There are other aspects of ionospheric dispersion, one of which is the splitting of the propagation into two propagation modes, the “ordinary” and “extraordinary” modes, due to birefringent refractivity of the ionospheric plasma in the geomagnetic field [*Jacobson and Shao*, 2001; *Massey et al.*, 1998b; *Shao and Jacobson*, 2001; *Shao and Jacobson*, 2002]. Both the primary pulse and the ground-reflection echo, in each spectrogram in Figure 1, clearly show the birefringent splitting, whose differential group delay varies in proportion to $1/f^3$.

The case examples of Figure 1 exemplify the two opposite ends of the somewhat bimodal distribution of VHF IC discharge signals seen with FORTE. The differences between these exemplars are:

- (a) Intensity: During emissions from the same storm, the intense pulses (Figure 1a; note color scale on right) show spectral density exceeding that of the weak pulses (Figure 1b) by typically two orders-of-magnitude.
- (b) Pulse-width: The intense pulses (Figure 1a) have intrinsic pulse-widths (of either the ordinary or extraordinary mode) on the order of a few μs , while the weak pulses (Figure 1b) have apparent pulse-widths at the limit of resolution (in the case of these spectrograms, $\sim 1 \mu\text{s}$).
- (c) Pulse shape: The intense pulses (Figure 1a) have an extended coda lasting several μs after the main pulse, while the weak pulses (Figure 1b) have no observable coda but instead terminate completely at the end of their main pulse.
- (d) Fading: The intense pulses (Figure 1a) exhibit deep and irregular amplitude modulation, or fading, between different frequencies within either birefringent mode. The fading bandwidth, or frequency separation between adjacent maxima and minima, is on the order of 1 MHz. By contrast, the weak pulses (Figure 1b) have much less fading; that is, the amplitude tends to remain more constant versus frequency within a given birefringent mode.

3. Single-pulse statistics of the FORTE IC pulses

3.1 Automated-selection tools for sorting RF pulses

In order to draw statistically meaningful conclusions about the distribution of intensity, pulsewidth, pulse shape, and fading, as well as about other parameters of interest, we have treated large numbers of FORTE data containing IC pulses with automated computational search algorithms that sort pulses according to various parameters. We shall apply selection criteria in two alternative ways.

3.1.1 Selection alternative 1: “Strong” pulses

We first impose selection criteria that accept only those IC pulses that dominate the background noise and whose TEC and echo delays can be easily ascertained. These criteria are described in general elsewhere [Jacobson *et al.*, 1999; Light and Jacobson, 2002]. Here we show how the pulse-acceptance criteria are applied to one example of a FORTE-recorded IC pulse, specifically the low-band signal whose spectrogram is in Figure 1(a). The signal is first dechirped (using the inferred $\text{TEC}=5.36 \times 10^{17} \text{ m}^{-2}$), then its carriers are suppressed, and finally a 1- μs -smoothed intensity (E^2 at the satellite versus time) is computed. This intensity is shown in Figure 2(a), for the entire 400- μs record (of which the presentation of Figure 1(a) is a portion). The first parameter we compute from the intensity is the “contrast”, defined as the ratio of peak to median intensity for that entire record. In this case the contrast is very large: 1791. Next, we compute the lagged autocorrelation function of the intensity, and this is shown in Figure 2(b). The main peak maximizes at zero lag and has a 1/e halfwidth of $\sim 5 \mu\text{s}$. The secondary peak at $\tau=55 \mu\text{s}$ corresponds to the delay of the ground-reflection echo. We compute the signal-to-noise ratio (SNR) of this peak relative to the statistical noise in the autocorrelation, estimated by the random variance outside of the main and secondary peaks. In this case, the SNR is quite large: 70.

The “strong” pulses in the following statistical study are selected by the following three criteria, all applied to the low-band signal:

- (a) Contrast > 50 .
- (b) SNR > 30 .
- (c) $E_{\text{max}}^2 > 2 \times 10^{-6} (\text{v/m})^{-2}$.

Together, these criteria (a-c) select 17,243 IC pulses. We call this selected cohort the “strong” pulses in what follows. Obviously, given that FORTE has recorded ~ 3 -million lightning pulses in the low band, this selection of “strong” pulses is extremely selective.

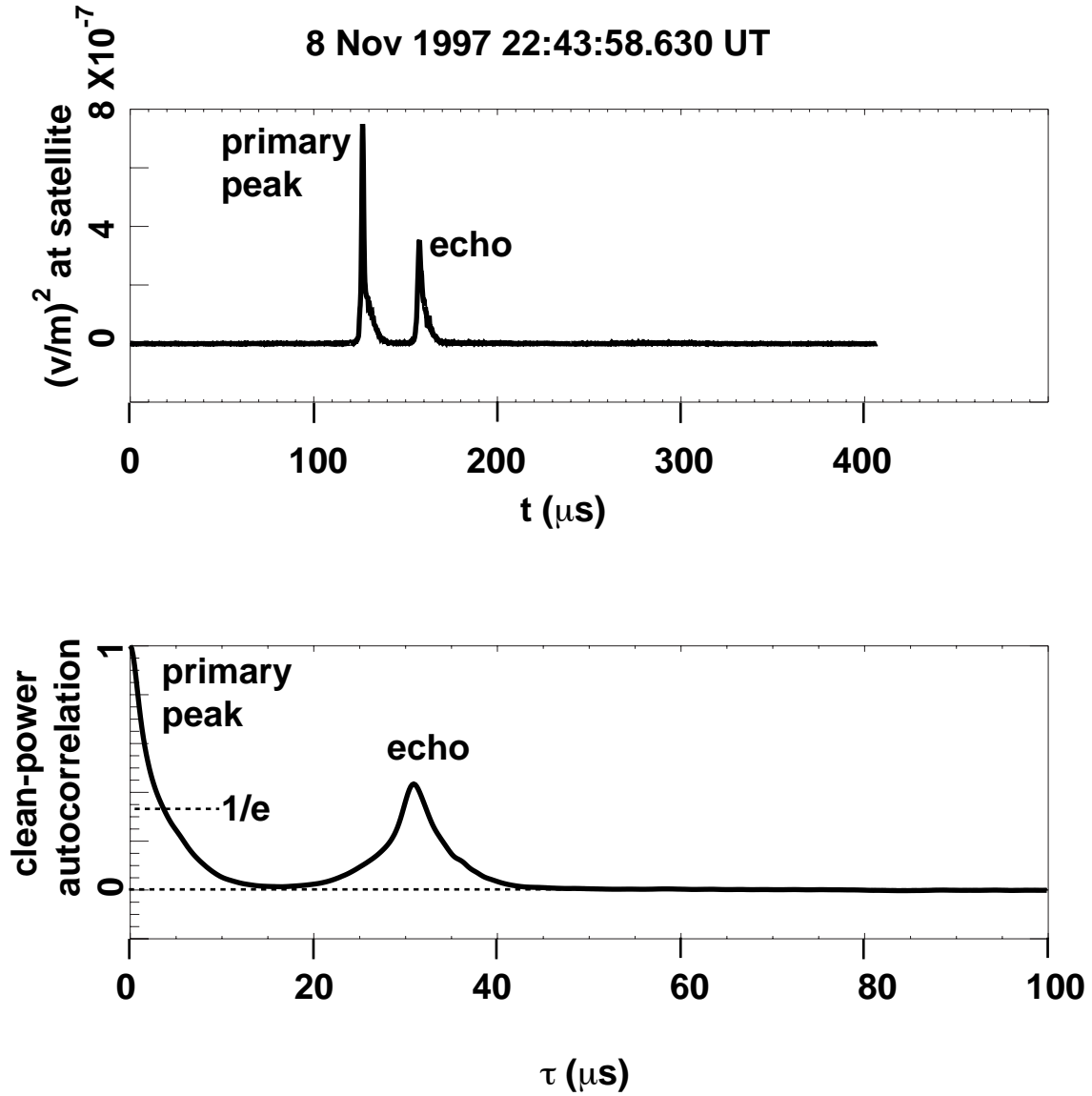


Figure 2: (a) Low-band intensity versus time for the strong pulse of Figure 1(a) above. Prior to evaluating the intensity $E^2(t)$, the carriers are suppressed, and the signal $E(t)$ is dechirped to first order. The echo is due to ground reflection. The “contrast” of the pulse is defined as the ratio of the peak to median intensity within the record. (b) Normalized autocorrelation function of the intensity shown in the top panel. The main peak’s halfwidth to $1/e$ furnishes a pulsewidth, and the signal-to-noise of the secondary peak furnishes a criterion (“snr”) for the ground-reflection echo’s readability.

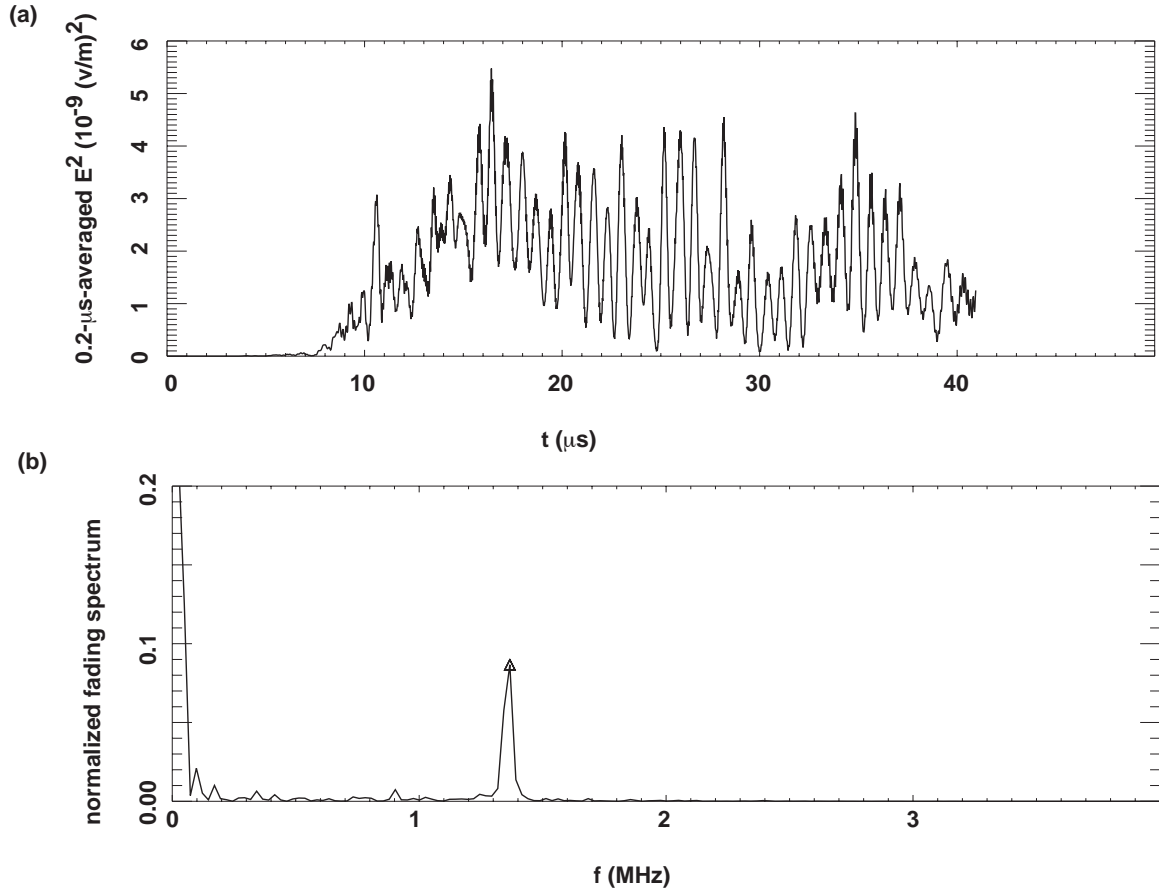


Figure 3: Illustration of amplitude modulation for polarized/coherent pulse of Figure 1(b) above. (a) 200-ns-smoothed intensity (E^2) versus time, showing regular periodic amplitude modulation. (b) Spectrum of intensity. Secondary peak at ~ 1.45 MHz corresponds to the regular periodic amplitude modulation.

3.1.2 Selection alternative 2: “Polarized/coherent” pulses

The second selection alternative is to analyze the mass of FORTE low-band IC pulse data for an entirely different pair of closely related characteristics, namely coherence and linear polarization. Coherence used here refers to the tendency of a signal’s spectrogram not to fade versus frequency, that is, for the fading bandwidth between adjacent maxima and minima to exceed the measurement bandwidth. The FORTE antennas are linearly polarized, and we have shown elsewhere how linear polarization of the incident RF radiation field can be determined in a simple, automated test by the response of a single linear antenna [Jacobson and Shao, 2001; Massey *et al.*, 1998b] if, and only if, the signal is also coherent. That is, if the signal is incoherent, or if the signal is randomly polarized, then the test we use yields a negative result. For a positive result to be obtained, the signal incident pulse must be both linearly polarized and coherent.

The coherence/polarization test is developed in detail in the Appendix but can be briefly indicated with reference to Figure 3. The top panel (Figure 3a) shows an example of the time history, during 2048 samples of 50-Megasample/s data, of the pulse intensity E^2 averaged with a sliding window 200 ns (i.e., ± 5 samples) wide. This signal is the primary pulse from Figure 1(b). The intensity shows a regular oscillation. The oscillation is almost full modulation of the intensity, and is also at a regular repetition rate, which together imply nearly perfect linear polarization [Jacobson and Shao, 2001; Massey *et al.*, 1998b]. The bottom panel (Figure 3b) shows the spectrum of the intensity, normalized to the value at zero frequency. The secondary spectral peak at $f \sim 1.45$ MHz rises distinctly above the neighboring noise in the spectrum. The secondary peak is a measure of the coherence and linear polarization of the incident field [Jacobson and Shao, 2001; Massey *et al.*, 1998b] and occurs at a frequency δf given by $\delta f = 2f_{ce} \cos\beta$, where f_{ce} is the electron gyrofrequency in the ionosphere, and β is the angle between the wavevector and the geomagnetic field in the ionosphere.

In order to select a cohort of IC pulses which exhibit the regular, narrow-band oscillation of Figure 3 and thus are likely both coherent and linearly polarized, the selection tool used (described in the Appendix) is applied to data like that in Figure 3, and selects 15,346 IC pulses that are likely to be both coherent and linear polarized. We will for brevity call this second cohort, of 15,346 IC pulses, the “polarized/coherent” pulses. These 15,346 are all comparable to the pulse of Figure 1(b) and Figure 3.

In order to indicate its selectivity, we apply the test for membership in the “polarized/coherent” pulse cohort to the example of the “strong pulse” shown earlier in Figure 1(a) and in Figure 2. The result is shown in Figure 4, which is analogous to Figure 3 except that it is applied to the primary pulse of Figure 1(a). The intensity modulation

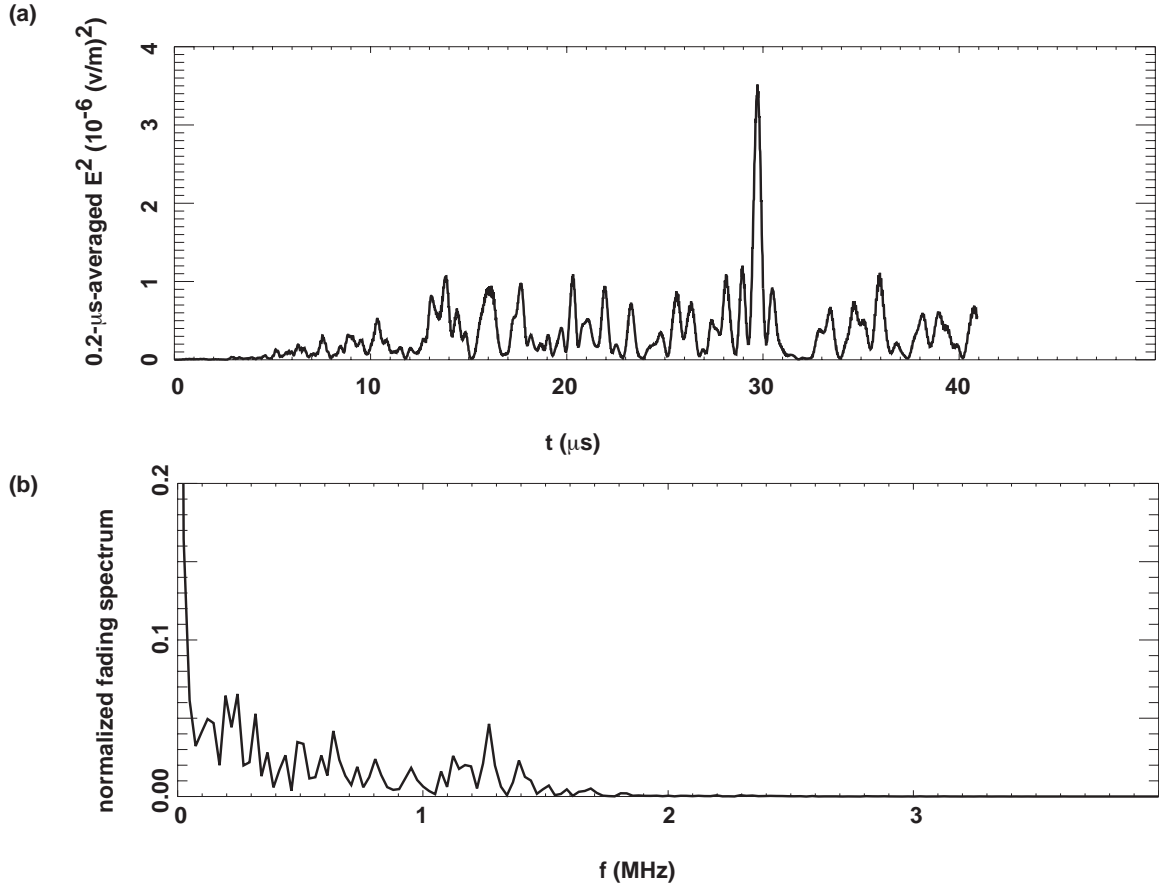


Figure 4: Illustration of amplitude modulation for strong pulse of Figure 1(a) above. (a) 200-ns-smoothed intensity (E^2) versus time, showing irregular amplitude modulation due to random fading. (b) Spectrum of intensity. There is no distinct or unique secondary peak in this case.

(Figure 4a) is irregular, rather than at a regular repetition rate. The modulation spectrum (Figure 4b) reflects this difference, being broad and irregular; the spectrum lacks a single modulation peak dominating over the noise in the spectrum. Thus, although a strong pulse, the example shown here robustly fails the polarization/coherence test (see Appendix for details). We emphasize that the pulse which passes the polarization/coherence test (Figure 1b and Figure 3) is almost a thousand-fold weaker in intensity than is the pulse which fails the polarization/coherence test (Figure 1a and Figure 4).

3.2 Determination of the pulsewidth

We use two methods of determining the pulsewidth, adapted to the very different properties of the strong pulses, on the one hand, and the polarized/coherent pulses, on the other hand. Specifically, we would ideally prefer to use the high-band to measure pulsewidths, due to the relative insensitivity of higher frequencies to ionospheric blurring. Therefore, the most relevant of the differences between the two classes of pulses is that the strong pulses have a relatively “white” spectrum compared to the polarized/coherent pulses. The practical consequence is that, during the recording of pulses with both low and high bands simultaneously, the strong pulses are more likely than are the polarized/coherent pulses to have a useable high-band signal. Approximately half of FORTE’s dual-channel [Jacobson *et al.*, 1999] pulse recordings are simultaneously at both low-band and high-band. For the polarized/coherent pulses, the high-band signal is so weak as to be unuseable. For the strong pulses, on the other hand, the high band provides a straightforward measure of the pulsewidth.

3.2.1 Pulsewidth determination for the strong pulses

The appearance of the strong pulses immediately indicates that they are always wider than 1 μ s. Thus a method of determining widths, to a resolution of 1 μ s, will not distort the width distribution for this cohort of pulses. The use of high-band data for automated determination of pulse-width easily avoids the confusion that birefringence and raybending introduce. Birefringent mode-splitting contributes a term varying as $1/f^3$, while raybending contributes a term varying as $1/f^4$, in the group delay [Roussel-Dupré *et al.*, 2001]. Taken together, these effects frequently blur pulses by as much as 10 μ s in the low band (38 MHz center frequency), and so one could not determine pulsewidths to within 1 μ s using a tractable automated procedure. However, the $1/f^3$ and $1/f^4$ scalings for these effects also guarantee that in the high band (~130-MHz center frequency) the blurring effect is small compared to the desired 1- μ s resolution. Thus, we will calculate pulsewidths using high-band data for the strong-pulse cohort, in which high-band data is furnished by the second receiver channel for about half the events. The pulsewidth is

determined in the same way as is illustrated for Figure 2, except rather than use the low-band intensity, we use the high-band intensity. Otherwise, prior to evaluating the intensity, the steps are the same: dechirping (but using the low-band-inferred TEC), and carrier suppression. The width is equated to the 1/e halfwidth of the intensity autocorrelation function's primary peak (see Figure 2b). Of the 17,243 strong pulses, 9034 have high-band signals and thus yield widths in this manner.

3.2.2 Pulsewidth determination for the polarized/coherent pulses

As mentioned above, the polarized/coherent pulses have relatively steep spectral roll-offs versus frequency and thus almost never have readable high-band signals. Therefore we must evaluate the pulsewidth, but using the low band, where lack of care in correcting for higher-order ionospheric blurring would render the results meaningless.

There is a highly accurate but also painstaking method for determining pulsewidth for dispersed low-band data, developed recently for the study of extremely narrow (<100 ns) VHF pulses associated with the initiation of negative cloud-to-ground strokes over seawater [Jacobson and Shao, 2002a]. The method uses low-band data, and must overcome the blurring effects of birefringence and ray-bending discussed in Section 2.2 above. Thus, this method has to be applied “by hand”, that is, with time-consuming user graphical interaction. Therefore, it can be practically applied to ~ 100 events but not to ~ 1000 or $100,000$. In order to apply it to a representative selection of polarized pulses, we will now drop the requirement that these pulses also meet the high-band requirements of moderately-strong events (see Section 3.1 above). This is reasonable since the polarized pulses tend to have weak, poorly readable, and frequently non-detectable high-band counterpart signals. Instead, we will select for exceptionally bright and readable low-band polarized IC pulse signals, *with no requirement for readable simultaneous high-band pulse signals*. Also, we do not restrict this search to FORTE events in which the high band is even recorded. Instead, we also consider those FORTE events in which both receivers are tuned to the low band. The selection criteria are described in the Appendix. Application of these criteria chooses 90 exemplary low-band coherent/polarized signals. We will call this cohort “very polarized” for short. About half of these very-polarized events do not even have a receiver at high band, and of those that have high band, most of the IC pulses in high band are unreadable due to their being too weak compared to the noise.

The method of determining pulse-widths for low-band data [Jacobson and Shao, 2002a] is briefly indicated here; see the Appendix for further details. Figure 5 shows spectrograms for the same low-band data that provides the polarized pulse seen earlier in Figure 1(b). The full 400- μ s recording (Figure 5a) is rendered with a 1.3- μ s temporal

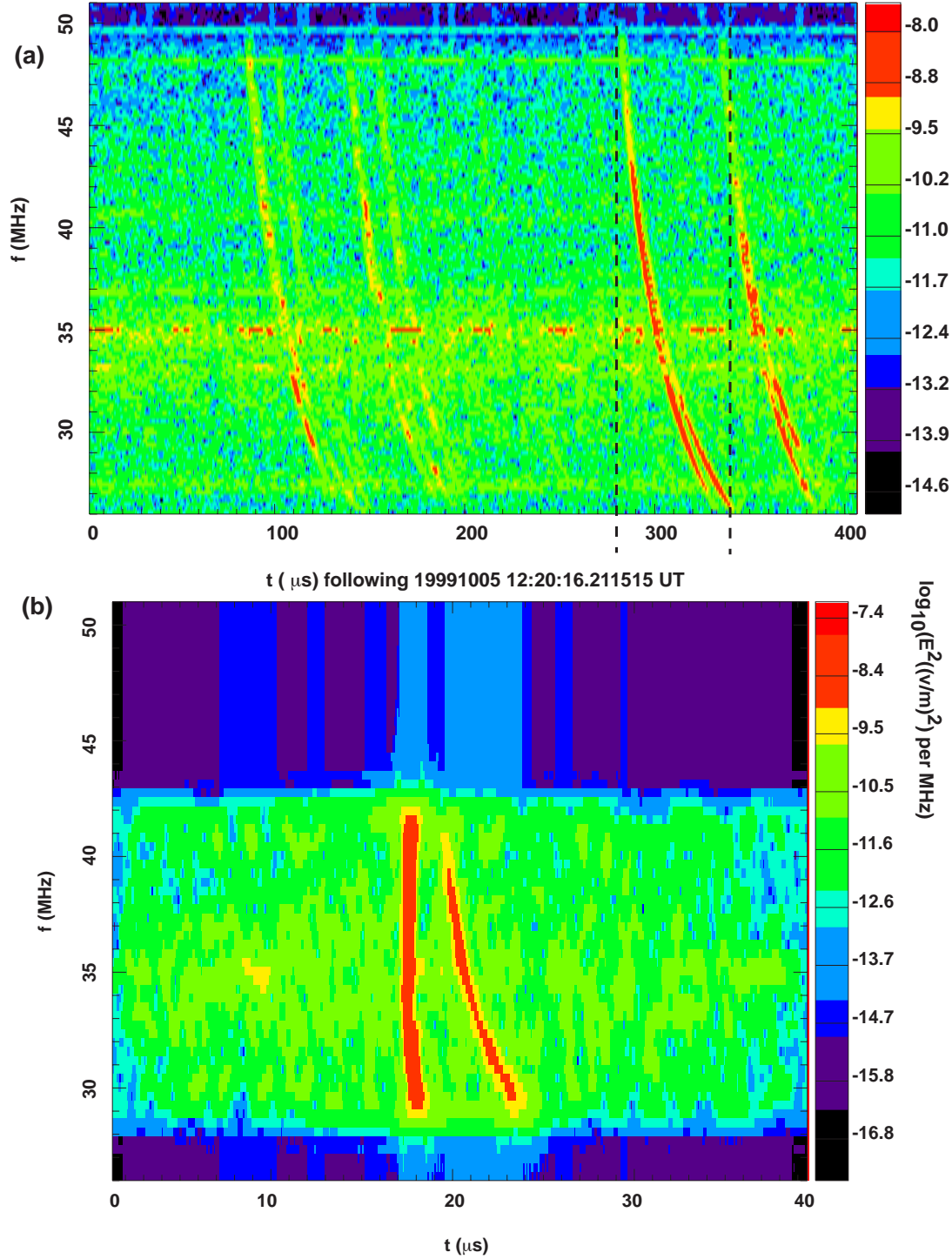


Figure 5: Spectrograms of polarized/coherent intracloud pulse shown earlier in Figure 1(b). (a) Entire 400- μ s record, with 1.3- μ s time resolution. The main pulse lies between the two vertical, dashed lines. (b) Detail of main pulse (from $t \sim 300$ μ s in (a)), after first-order dechirping for ordinary mode, with 0.6- μ s time resolution. The 40- μ s time range is centered on the main pulse.

resolution. Between $t=100\ \mu\text{s}$ and $t=200\ \mu\text{s}$ are two interleaved IC pulse pairs. Later, after $t=280\ \mu\text{s}$, is a single and stronger pulse pair. The initial pulse in this latter pulse pair is examined more closely in Figure 5(b), where there are now three differences in treatment: (1) The spectrogram temporal resolution is now $\sim 0.6\ \mu\text{s}$. (2) The signal has been dechirped prior to forming the spectrogram, to compensate approximately for the main dispersion varying as $\sim \text{TEC}/f^2$ [Jacobson *et al.*, 1999; Jacobson and Shao, 2002a], which is the first-arrival pulse. (3) The parts of the spectrum in which the pulse is very weak (below 29 MHz) or in which the two modes are overlapping (above 42 MHz) are suppressed. The computer algorithm then analyzes the ordinary-mode spectrogram feature to determine the residual dispersion remaining in the ordinary mode. After parametrizing the residual dispersion, and already knowing the main dispersion that varies as $\sim \text{TEC}/f^2$, the algorithm returns to the original time-series data and corrects for both effects, resulting in an optimally dispersion-corrected signal for the ordinary mode. The temporal resolution of this method is on the order of the inverse of the effective bandwidth, which after application of the filter (see above) is on the order of 10 MHz, resulting in a temporal resolution of $\sim 100\ \text{ns}$. The fully dispersion-corrected low-band signal is then fed into the same procedure for determining the $1/e$ width of the autocorrelation function of the intensity, that was previously applied to high-band data for the strong pulses. This method is applied to 90 exemplary pulses from the polarized/coherent pulse cohort. The criteria for selecting down to just 90 pulses to analyze are listed in the Appendix.

3.3 Comparison of pulsewidths for the strong and the polarized/coherent pulses

The joint results of the two pulsewidth-determination methods are shown in Figure 6, which presents histograms of $1/e$ pulsewidth for both the strong pulses (solid curve) and the 90 hand-analyzed polarized/coherent pulses (dashed curve). The abscissa is logarithmic, the bin size is 40 ns, and the two histograms are separately normalized.

The clear result in Figure 6 is that the moderately strong pulses have several- μs pulse widths, while the very polarized pulses have $\sim 0.1\text{-}\mu\text{s}$ pulsewidths. (The $0.1\text{-}\mu\text{s}$ pulse width is an upper bound on what the true width would be with wider-band recordings, because of the $0.1\text{-}\mu\text{s}$ resolution imposed by the typical effective bandwidth of 10 MHz after filtering.) The pulse-width behavior of IC discharge pulses is utterly bimodal.

The several- μs width of the strong pulses confirms that the $1\text{-}\mu\text{s}$ resolution in determining that cohort's widths is not a significant limitation. Moreover, the bandwidth-limited pulsewidth of the polarized/coherent pulse cohort is consistent with the earlier assertion that they lack intrapulse fading, i.e. that they are coherent.

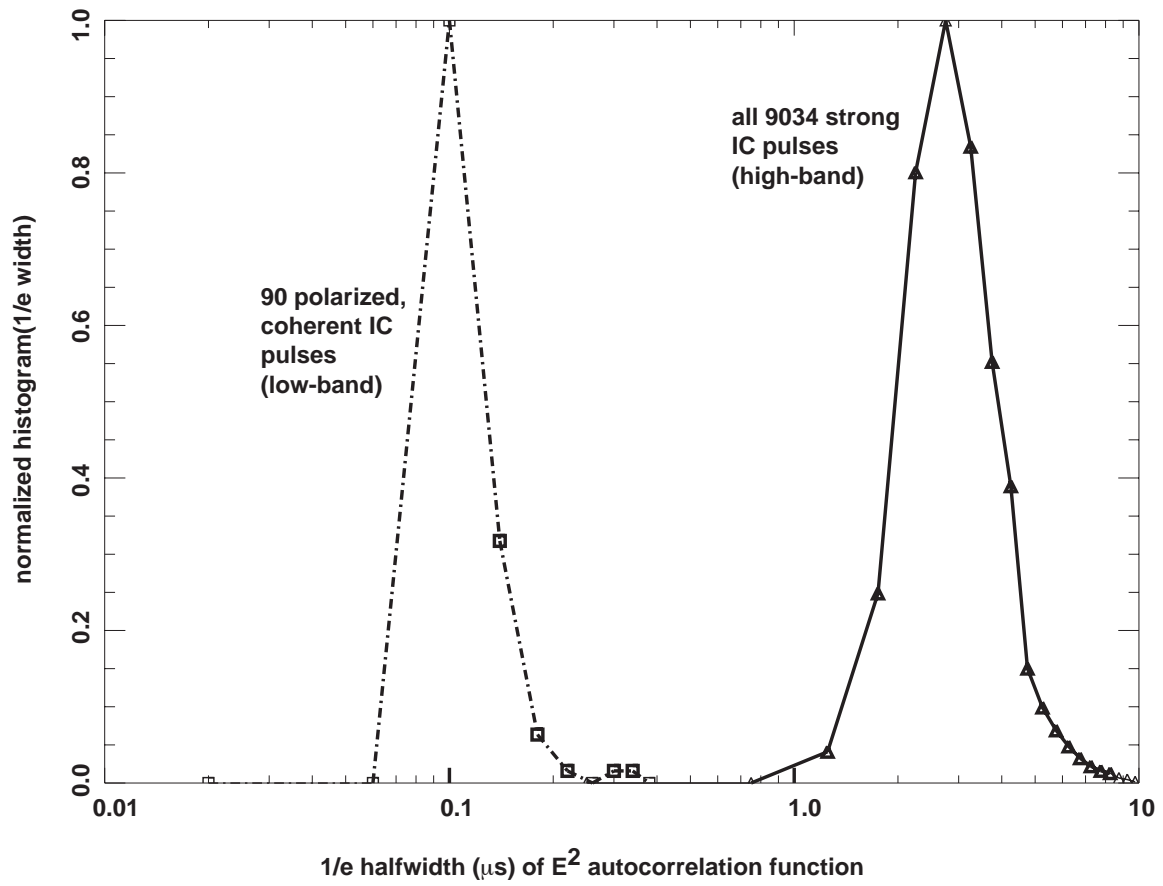


Figure 6: Normalized histograms of intensity autocorrelation function 1/e halfwidth, for all 9034 strong pulses (solid curve, using high-band) and for the 90 exemplary polarized/coherent pulses (dashed curve, using low-band).

4. Relationship of FORTE IC pulses to other pulses in the same flash

4.1 Method for identifying flashes

FORTE triggers do not occur randomly in time, but rather tend to appear as members of bunches or clusters. These clusters correspond to lightning “flashes”.

For a given IC pulse or “key” event, we wish to determine the relative timing and characteristics of neighboring events within the same flash that contains the key event. Ordinarily we associate IC emission pulses within ~ 0.5 s of each other, as belonging to the same IC flash. If the rate of triggers arriving at FORTE is sufficiently small, compared to 2 pulse/s, then merely having two pulses received with an interval much smaller than 0.5 s suggests that they are from the same flash.

However, there is a pitfall in associating pulses with each other merely on the basis of their being temporal neighbors. Unlike the LMA [*Rison et al.*, 1999; *Thomas et al.*, 2001] and other ground-based lightning mapping systems, and unlike fine-resolution optical imagers [*Boccippio et al.*, 2000a; *Christian et al.*, 1999; *Suszcynsky et al.*, 2000b], a single satellite like FORTE recording a VHF pulse cannot spatially locate that pulse. In particular, some apparent neighboring pulses, though close in time, may arise from altogether different storms in the large field-of-view. To avoid making such a mistaken association of pulses from widely-separated storms into the same flash, we exploit a comparison of TEC, which is automatically retrieved during the data reduction and is stored for later use. The TEC varies sensitively with storm position [*Jacobson et al.*, 1999; *Jacobson and Shao*, 2002b; *Tierney et al.*, 2001] and usually can be compared in order to determine whether two temporally-neighboring pulses indeed came from the same storm. More precisely, we require that two pulses that are temporal neighbors be considered to belong to the same flash only if their TEC values are also in sufficiently close agreement. This is used to narrow our pool of candidate neighbor pulses in what follows.

4.2 Observed probability of same-flash neighbors

The first thing to establish is the likelihood of any randomly chosen FORTE VHF “key” event being accompanied by a neighbor in the same flash, as a function of the time separation of the neighbor from the key event. This is shown in Figure 7, which is the observed probability of there being a same-flash neighbor per 0.01-s separation bin. Figure 7(a) shows this probability on the basis of all VHF key events. This is a larger set than either the strong- or polarized/coherent-pulse cohorts. This larger set comprises all FORTE VHF events in which TEC is reliably determined.

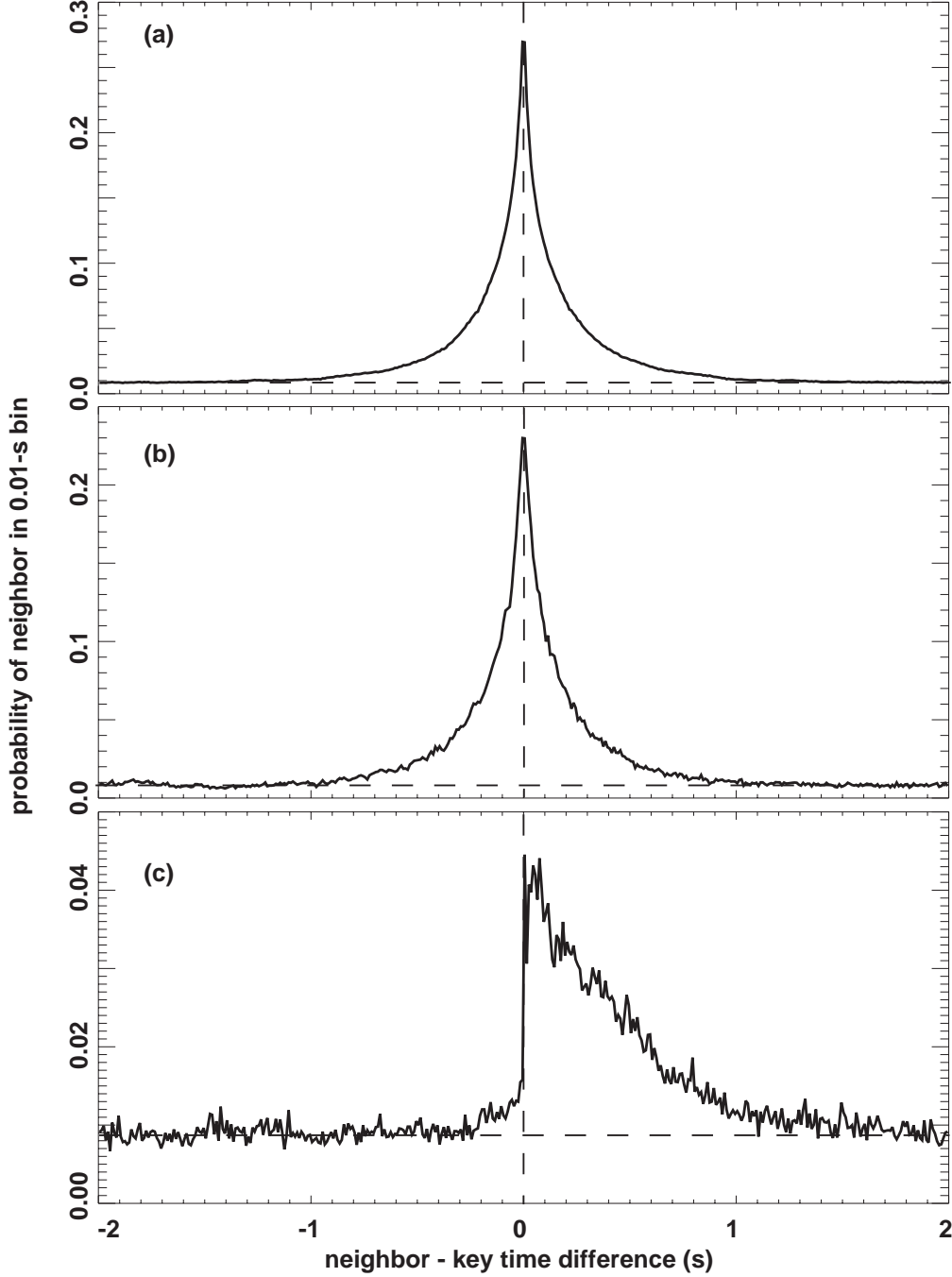


Figure 7: Observed probability of there being a same-flash neighbor per 0.01-s separation bin. The neighbor candidate pool comprises all FORTE VHF events having a low-band channel and having a well-determined TEC, without requiring either strong or polarized/coherent pulses (see text). (a) The key-event pool is the overall pool also used as neighbor events. (b) The key-event pool is restricted to the 15,346 polarized/coherent events (see text). (c) The key-event is restricted to the 17,243 strong events (see text).

The horizontal dashed line in Figure 7 (a) indicates the level of statistical noise below which the probability is entirely accidental (due to residual overlap of essentially unrelated flashes, despite the requirement for agreement in TEC). That level is determined by the flat baseline due to accidental coincidences [Jacobson *et al.*, 2000] that are independent of time separation. Superimposed on this accidental baseline in Figure 7(a) is a compact flash signature with characteristic width < 1 s. Given a VHF key event, the most probable VHF neighbor separation is within ± 0.01 s, and the probability monotonically declines as the separation increases. The distribution in Figure 7(a) will be considered a control case, because no particular pulse characteristics have been required of the key event. Rather, Figure 7(a) describes the probability of VHF neighbors for the key events' being the entire parent distribution of VHF events.

Next, we calculate the neighbor probability again, but with the key events' being limited to the 15,346 polarized/coherent pulses. The candidate pool of neighbors, however, remains the larger set (that was the source of both neighbors and key events in Figure 7a). Figure 7(b) shows the probability of neighbors in 0.01-s time-separation bins, based on the polarized/coherent key events only. Apart from increased statistical noise (due to a smaller sample of key events), the probability in Figure 7(b) is extremely similar to that in Figure 7(a). The conclusion is that in terms the probability of neighbors (as a function of neighbor-key time separation), the polarized/coherent cohort of pulses do not behave very differently from the entire background distribution of VHF events: Both are highly likely to have neighbors in ± 0.5 s, and the probability distribution is symmetric. This latter finding indicates that the polarized/coherent key event has no favored position within a flash; it is equally as likely to precede, as to follow, its same-flash neighbors.

The tendency of polarized/coherent pulses to have flash neighbors is underlined by the example of polarized/coherent pulses in Figure 5(a). Even the brief (400- μ s) record duration contains three recognizable pulse pairs (plus numerous weaker emissions). This indicates that the method used to prepare Figure 7 results in an underestimate of the number of neighbors belonging to a pulse, because the neighbors within the same record cannot be counted.

Finally, we calculate the neighbor probability yet a third time, but now with the key events restricted to the 17,243 strong IC pulses. Figure 7(c) shows the probability of neighbors (from the entire parent distribution of VHF events) in 0.01-s time-separation bins, based on the strong IC key events only. Now the probability distribution dramatically departs from the behavior in Figures 7(a,b). The strong IC pulses are fivefold less likely to have same-flash neighbors, *but when there are neighbors, they tend to occur after the strong IC pulse key event.*

We conclude from Figure 7(c) that the strong *IC pulses are an initiatory process in a flash*, and that the strong IC pulses do not recur within a flash. A strong IC pulse either occurs at the very start in a flash, or does not occur in a flash at all. If it occurs in a flash, it is never preceded in that flash by previous same-flash neighbors.

We note that the accidental-coincidence baseline in Figure 7(c) (at a level of ~ 0.009 per 0.01-s bin) is similar to what it is with the control (Figure 7a) and the polarized/coherent (Figure 7b) key events. However, the accidental-coincidence is now five times as large relative to the diminished peak probability. In order to improve this peak/accident ratio, we next select for quieter storm settings, in which FORTE is not receiving a very high trigger rate from multiple storms having the same TEC. To do this, we select only those key events that have no neighbors during the preceding 2 s. (Figure 7c justifies us in doing this, because the probability of non-accidental neighbors is essentially zero before the key event. All that we stand to lose is some of the accidental time neighbors.) Of the original 17,243 key events, we now retain only the 10,432 that lack neighbors during the preceding 2 s. This subset of key events will be used in the next sub-section.

The presence of neighbors only after, but not before, a strong IC pulse key event indicates that these the strong IC pulses are initiators of IC flashes. This is consistent with the findings from the LMA [*Rison et al.*, 1999; *Thomas et al.*, 2001].

4.3 Further statistics of same-flash neighbors following strong IC pulses

We now restrict our attention to the neighbors following the 10,432 key events developed as a subset of the key events of Figure 7c. Further, we additionally restrict the set of neighbors to those that occur within 0.6 s following any of those 10,432 key events. This choice is motivated by Figure 7(c), which makes clear that most of the non-accidental neighbors occur during that time interval. We find that of the 10,432 key events, there are 4864 key events that lack any neighbor within the following 0.6 s. Thus, almost half of the strong-pulse key events occur in isolation. The other 5568 key events have, on average, ~ 2 neighbors each. The distribution of the number of neighbors in the 0.6 s following these other 5568 key events is shown in Figure 8. The distribution shows that there is not a standard, unique number of neighbors. Rather, the most probable number of neighbors is one, but on the other hand there are instances of dozens of neighbors too. We infer that the initiatory event (the strong pulse at the head of the flash) does not always successfully trigger a flash. Some flashes are initiated but never sustained as a propagating leader. Other flashes are initiated and then provide copious bursts of pulses.

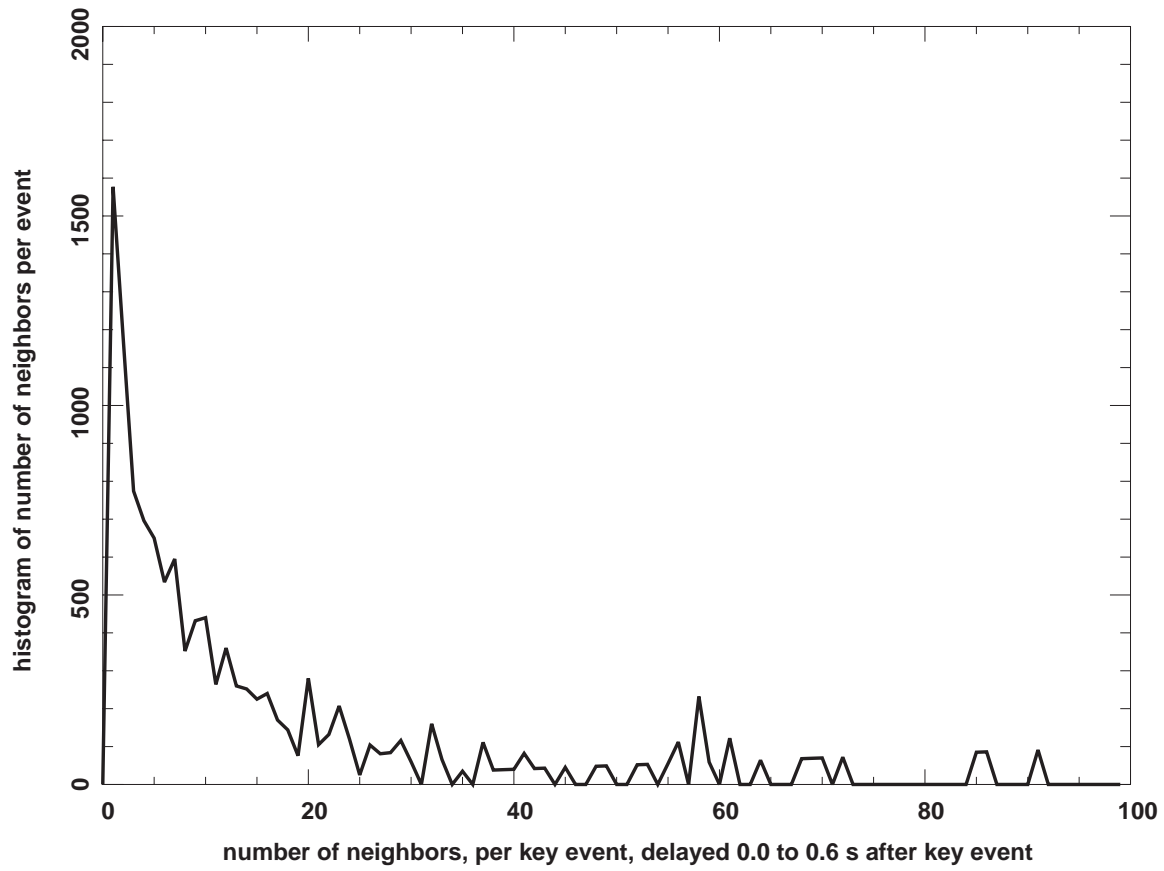


Figure 8: Histogram of the total number of neighbors per strong-pulse key event within 0.0 to 0.6 s after key event. The key events are restricted to those strong IC pulses having neighbors in the following 0.6 s but no neighbors in the preceding 2.0 s.

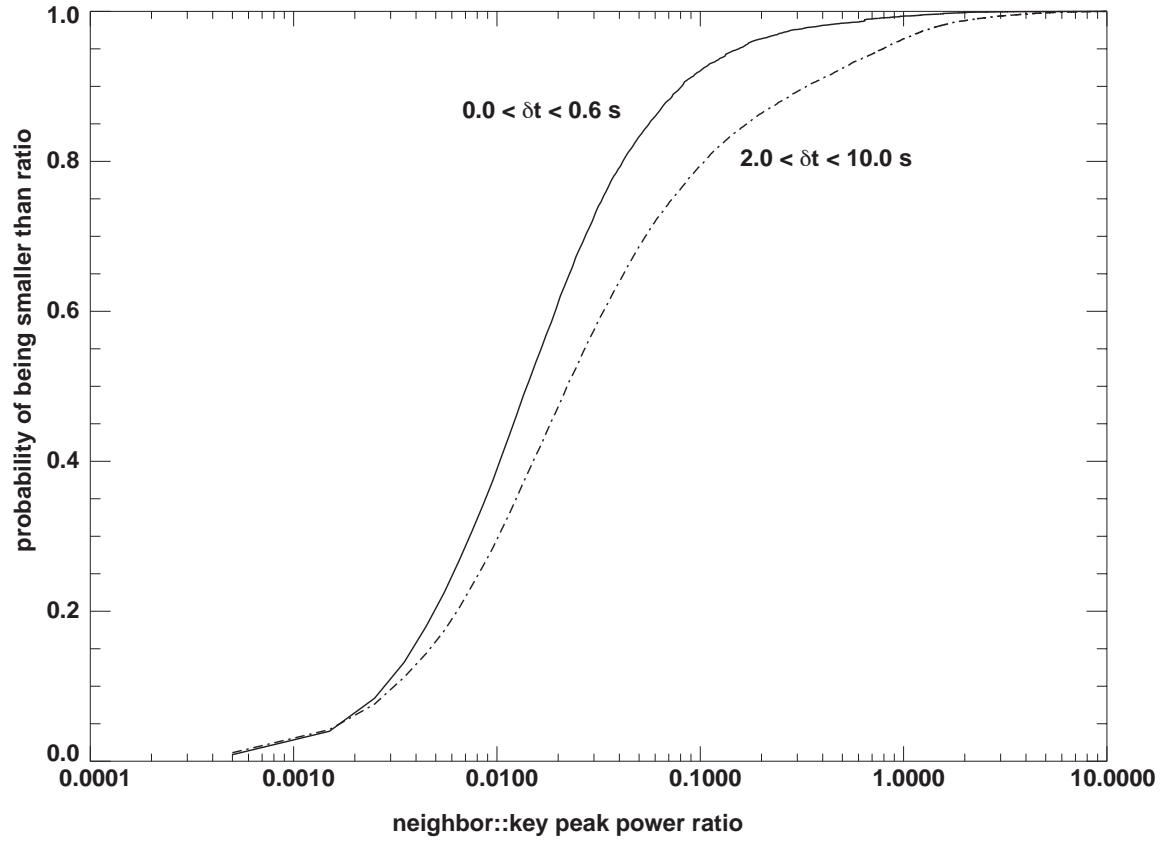


Figure 9: Cumulative probability of neighbor-to-key low-band peak-power ratio, for neighbors within 0.0 to 0.6 s after key event (solid curve) and for neighbors within 2.0 to 10.0 s after key event (dashed curve). The key events are restricted to those strong IC pulses having neighbors in the following 0.6 s but no neighbors in the preceding 2.0 s.

We now compare the peak power of the neighbors following the key events to the peak power of their respective key events. Figure 9 shows the cumulative distribution of this power ratio, for neighbors within 0.0 to 0.6 s (solid curve) and within the range 2.0 to 10.0 s (dashed curve). It is clear that the 0.6-s neighbors are very weak compared to the preceding key event. For example, 97% of these neighbors have less than 0.1 of the peak power of their preceding key event. The more distant neighbors, in the time delay range 2.0 to 10.0 s, show somewhat higher power than do the close-in neighbors. This is probably due to the recurrence of a small number of strong IC pulses like the key event, but only after a “recovery” time that apparently exceeds 0.6 s. The only neighbors within 0.6 s are pulses whose intensity is weak compared to the IC pulse key events.

We now examine the development of an individual flash in which there is an initiatory IC strong pulse followed by >30 neighbors. In particular, we examine the intensity and emission-height relationship between the initiatory pulse and the subsequent neighbors. The emission-height relationship can be inferred from the pulse-pair time separation, which is proportional to emission height [Jacobson *et al.*, 1999].

Figure 10 shows (a) the pulse-pair time separation versus time and (b) the pulse intensity versus time. The symbol size is proportional to the pulse intensity. The first pulse, which is the key event in the flash, is labeled “initiator” in both panels of Figure 14. The pulse-pair separation increases about 30% going from the initiator pulse to the first weak neighbor pulse, and then remains steady for the remainder of the flash. This pattern has been seen frequently by the LMA [Rison *et al.*, 1999, e.g., see their Figure 7, top panel], and has been interpreted as the propagation of negative stepped leader breakdown into a horizontal layer of positive charge that is located above the initiator breakdown.

5. Shape of the polarized/coherent pulses

The data discussed above are consistent with the the weaker, more polarized, and more coherent pulses’ being manifestations of discrete leader steps in IC flashes. Is their remarkably narrow and coherent (i.e., non-fading) pulse-shape also consistent with what is known about discrete leader steps? Wideband (0-20 MHz) sferic measurements [Willett *et al.*, 1990; Willett and Krider, 2000] of fast vertical-electric-field transients, situated so as to ensure that the propagation path to the sensor was over highly-conducting seawater, have revealed that discrete leader steps give rise to a coherent monopulse of ~ 100 -ns width (in dE/dt). Indeed, this discrete leader-step monopulse is hardly distinguishable in appearance [Willett and Krider, 2000, see the pulse taxonomy in their Figure 1] from the sferic associated with initiation of negative cloud-to-ground strokes on seawater. Only the context distinguishes them: The discrete leader step is accompanied (in time) by other

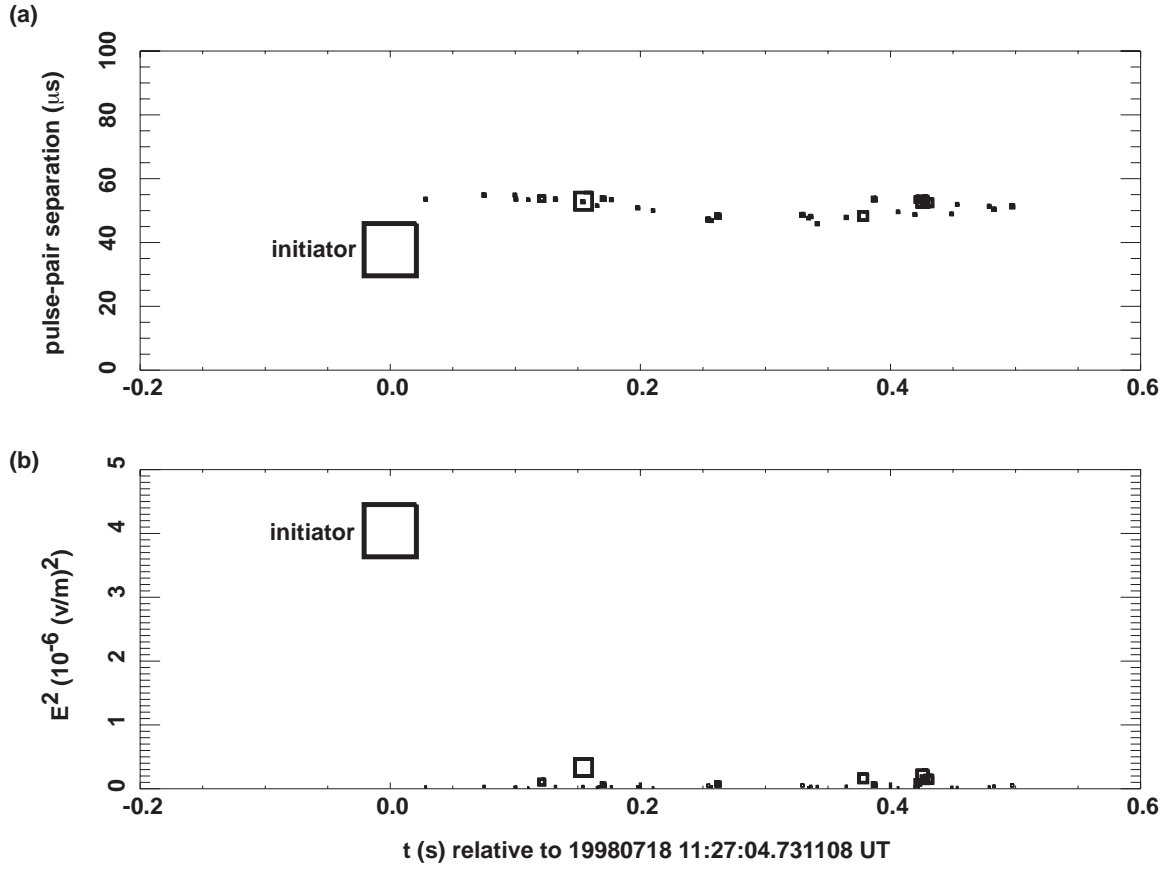


Figure 10: Development of an intracloud flash initiated by a strong IC pulse. (a) Pulse-pair separation (proportional to emission height) versus time. (b) Low-band peak intensity versus time. The symbol size is proportional to intensity.

leader steps, while the negative cloud-to-ground strokes on seawater is isolated for tens of ms from repetitions of like pulses. Not coincidentally, the initiation of negative cloud-to-ground strokes on seawater also generates a VHF signature that is narrow, polarized, coherent, and steep-spectrum [Jacobson and Shao, 2002a].

6. Shape of the strong pulses

The distribution of pulse widths in Figure 6 indicates that the strong, flash-initiating IC pulses have overall pulsewidths on the order of a few μs . The method used in deriving those distributions is the intensity autocorrelation function (after dechirping the signal). That method cannot discriminate between various alternative pulse shapes that give the same autocorrelation width. In order better to convey the shape of these strong IC flash-initiator pulses, we present in Figure 11 the dechirped high-band intensities as a function of time for 14 successive strong IC flash-initiator examples in the list of those which are followed by neighbors within the subsequent 0.6 s. The vertical axis is logarithmic (and offset, so that absolute intensity cannot be inferred from the figure), while the horizontal axis is linear in time. The intensity is smoothed by $\pm 0.1 \mu\text{s}$. The intensity risetime is on the order of $1 \mu\text{s}$. The intensity is sustained at near-peak value for a few μs , then falls over a timescale of several μs , frequently transitioning to a slower rate of decay at very low power. There is generally no precursor emissions before the $1\text{-}\mu\text{s}$ rise portion of the pulse. The “noisy” variations of the intensity, even near the peak and far above the background noise, are consistent with the fading seen on the spectrogram of Figure 1(a). We interpret this noise-like fading of strong IC initiator pulses as evidence for their being a superposition of emissions from numerous emitters, spatially separated and mutually unsynchronized from each other. The presence of numerous, nearly-simultaneous emitters of random orientation, even if the emitters themselves were individually linear dipoles, would provide a net radiated field that is randomly polarized fading [Jacobson and Shao, 2002b, see their Figure 2].

7. Relationship of strong IC pulses recorded by FORTE to NBEs recorded by a ground-based sferic array

The FORTE project team has operated a small, specialized sferic-waveform array [Smith *et al.*, 2001] in Florida to assist in the understanding of FORTE signals arising from storms in the area. Each station of the array has a capacitive sensor of vertical electric-field perturbations. The sferic-waveform array processor determines the horizontal

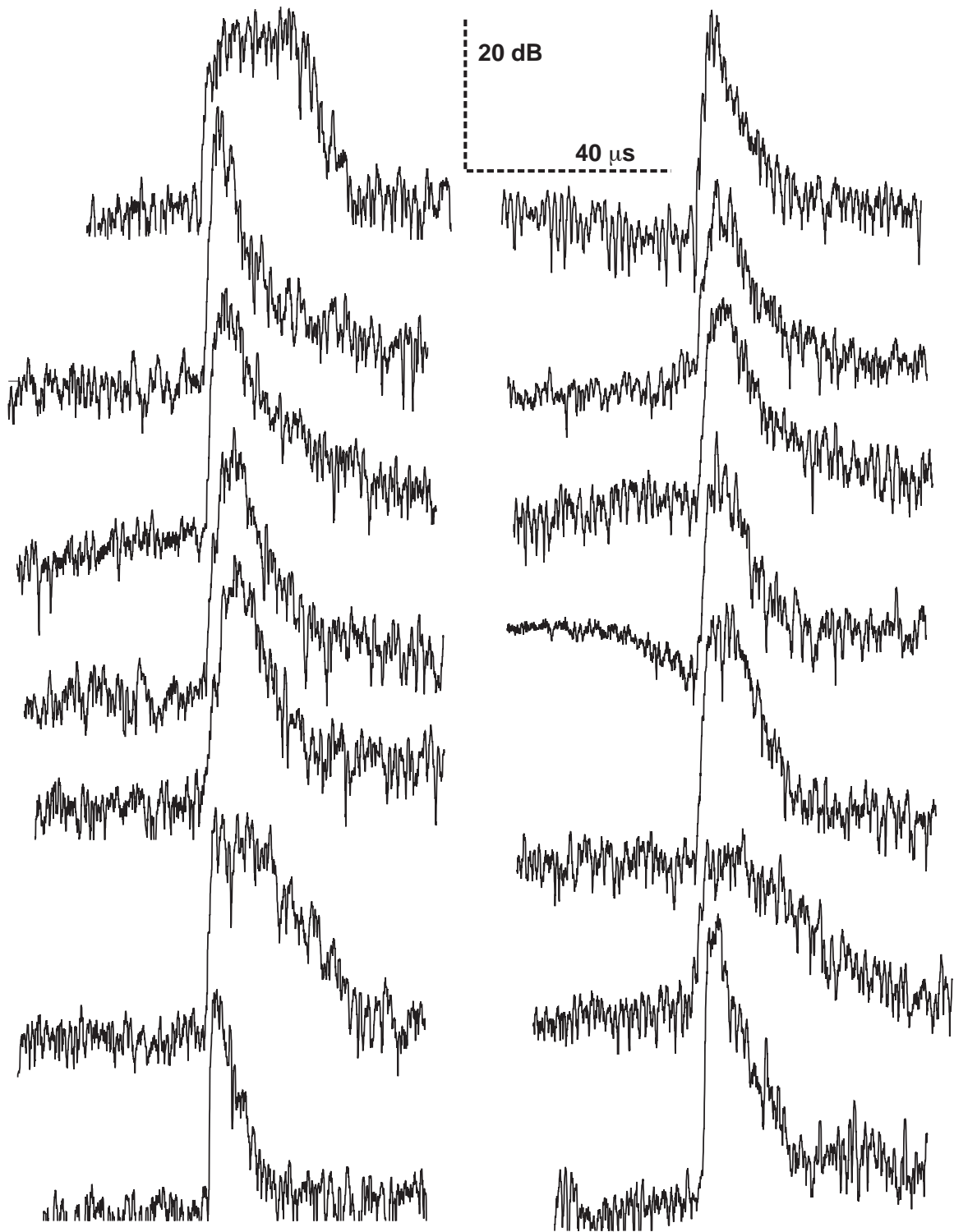


Figure 11: Overlay of 14 successive strong-pulse intensities versus time, with a logarithmic vertical scale.

location (by time-difference-of-arrival) of lightning strokes within the array's effective range (several-hundred km), and archives the various participating stations' full waveforms of the recorded VLF/LF signals. These waveforms are sampled at 1 megasample/s; typical recorded records are 8.192 ms long (8192 samples). Figure 12 shows three typical 0.6-ms sections of sferic waveforms. Figure 12(a) shows a positive NBE (NPBE), Figure 12(b) shows a negative NBE (NNBE), and Figure 12(c) shows a conventional sferic. The NPBE and the NNBE both exhibit the pair of echoes (the first from an ionospheric reflection, and the second from a ground reflection and then an ionospheric reflection) which can be used to retrieve the stroke altitude [Smith *et al.*, 1999].

There have been 2439 close coincidences of FORTE VHF events and sferic-array LF strokes. Figure 13 shows histograms of the sferic-FORTE time difference, for (a) the 1943 sferics that are "conventional", and (b) the 496 sferics that are NBEs. The latter show a narrow distribution of the relative emission time which is consistent with correlation of FORTE-detected VHF emissions and both a small number of IC strokes, and a larger number of cloud-to-ground strokes, detected by the National Lightning Detection Network [Jacobson *et al.*, 2000]. Figure 13(b) clearly demonstrates the close association between NBEs and IC pulses observable by FORTE. The slight shift, and finite width of the time-delay distribution in Figure 13(b) are not big enough to be clearly physical in origin. The errors in knowledge of FORTE's instantaneous position, on the order of ~ 10 km, introduce errors of ~ 30 μ s in the VHF event timestamps, even after extensive correction for propagation delays [Jacobson *et al.*, 2000]. These errors, which may have systematic as well as random components, may account for all of the asymmetry and spread of the time-delay distribution between the sferic and the VHF signals. That is, the distribution shown in Figure 13(b) is consistent with, but cannot prove, the hypothesis that the LF and VHF emissions are synchronous.

We note that the published ground-based, coordinated measurements [Smith *et al.*, 1999, see their Plates 1 and 2] of both the LF signals of NBEs, and the associated HF signals, indicate that the HF pulse duration was ~ 10 μ s and that it was centered on the first half-cycle of the NBE pulse. Because of this, we conclude that the measured spread in NBE-versus-FORTE time differences (Figure 13b) is due to a combination of the errors in the sferic-waveform-array geolocation and the ~ 10 -km random uncertainties in FORTE location.

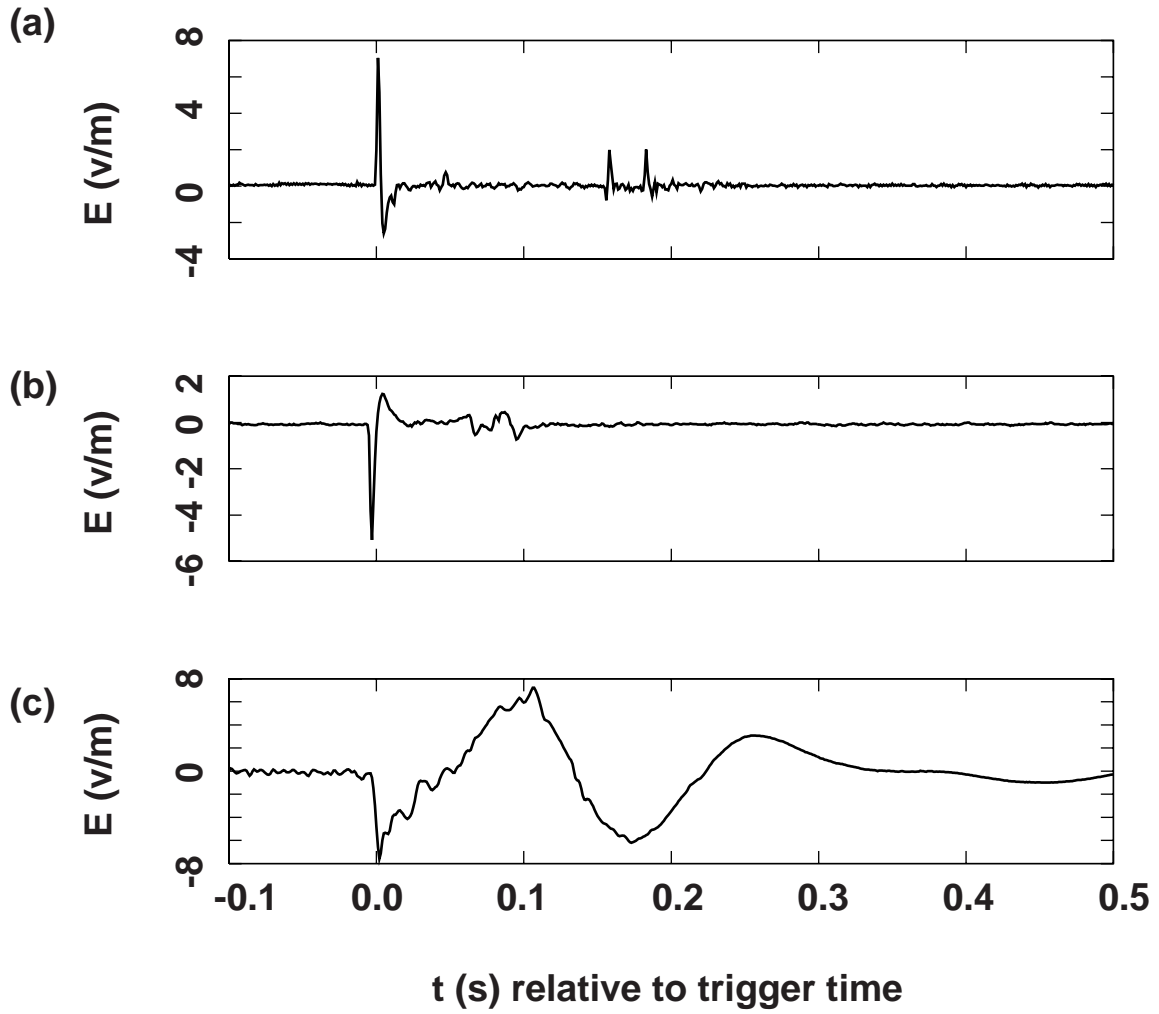


Figure 12: Los Alamos Sferic Waveform Array vertical electric field data examples for (a) a Narrow Positive Bipolar Event (NPBE), (b) a Narrow Negative Bipolar Event (NNBE), and (c) an ordinary sferic.

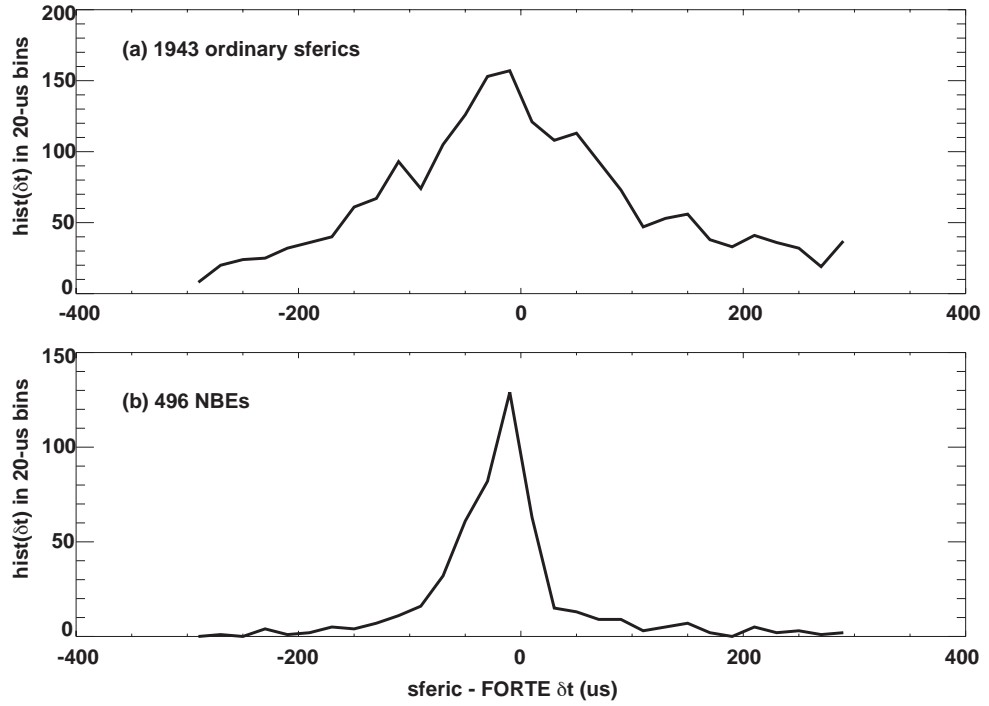


Figure 13: Histograms of {sferic -origination time} minus {FORTE VHF signal-origination time}, for (a) 1943 ordinary sferics, and (b) 496 Narrow Bipolar Events.

8. Summary

The numerous intracloud RF pulses recorded by FORTE contain two distinctive types of signatures. These types are called “strong”, and “polarized/coherent” respectively. They exhibit widely differing characteristics as follows:

- (a) Emission intensity: The strong pulses as a group have intensities that are two (and sometimes three) orders-of-magnitude greater than the polarized/coherent pulses.
- (b) The strong pulses as a group are randomly polarized, whereas the polarized/coherent pulses show linear polarization when their signal-to-noise permits determination of the polarization.
- (c) The strong pulses as a group are either isolated in time, or serve as initiators of flashes whose subsequent emissions are not as strong and are frequently polarized/coherent. By contrast, the polarized/coherent pulses can occur anywhere in an IC flash and are not uniquely observed as initiators of flashes. Moreover, the polarized/coherent pulses are usually accompanied closely in time by other pulses of the same type.
- (d) The strong pulses as a group show deep fading within the pulse, whereas the polarized/coherent pulses have a simple, coherent monopulse structure.
- (e) The strong pulses are very wide ($\sim 3\text{--}5\ \mu\text{s}$) compared to the polarized/coherent pulses ($\sim 0.1\ \mu\text{s}$).
- (f) The strong pulses are the most likely RF pulse to accompany simultaneous Narrow Bipolar Events on LF/MF recordings of the radiation-field vertical electric field (sferic) near the ground. By contrast, the polarized/coherent pulses have no special simultaneity or preferred association with Narrow Bipolar Events.

The strong pulses have been shown elsewhere to tend to be unaccompanied by light emission that is observable from space. This raises the possibility that the strong RF pulse could provide a remote-sensing complement to optical signals of lightning. That is, as an indicator of IC lightning, the strong/unpolarized pulse is perhaps not redundant with optical signals.

Of these two types of IC lightning RF signatures, the strong pulse has the greater likelihood of satisfying trigger requirements in the presence of competing background noise, for RF sensors on a satellite constellation. We stress the importance of understanding the strong pulses’ meteorological setting, a work that has just begun [Smith *et al.*, 1999].

Appendix

A1. Automated search algorithm for polarized/coherent pulses

The search for, and characterization of, possible polarized/coherent pulses are done with an automated algorithm capable of treating each FORTE VHF event (400- μ s record) in typically about 2 s of elapsed time. Since there are about 3-million FORTE VHF events with low-band data that need to be examined, the search algorithm has had to work on the data for 6-million seconds, or over two months. The algorithm is based on the unique and distinguishing feature of polarized/coherent pulses that, following transionospheric propagation, their intensity is amplitude-modulated at a steady rate proportional to the electron gyrofrequency in the ionosphere. The derivation of that result can be found elsewhere [Jacobson and Shao, 2001; Massey *et al.*, 1998b]. Essentially, the TEC/f^2 dependence of the overall group retardation, coupled with the $\text{TEC}Xf_{ce}\cos(\beta)/f^3$ dependence of the birefringent splitting [Jacobson and Shao, 2001; Massey *et al.*, 1998b], together produce a progressive rotation of the linearly-polarized electric-field vector at the antenna. Since the antenna is linearly polarized, the result is an intensity modulation at twice the rotation frequency.

Owing to the fact that the coherent/polarized pulses tend to weak, the algorithm must be as robust as we can make it against the effects of anthropogenic background noise and signals. A modulated carrier wave can mimic the amplitude modulation from transionospheric propagation; this effect must be rejected in the analysis.

The automated algorithm's steps are as follows:

Step 1: We wish to identify the strongest lightning pulse in the record. and to reject non-lightning pulses, such as radar signals, that can also be in the record. After suppressing anthropogenic carrier waves [Jacobson *et al.*, 1999], the algorithm computes the 2- μ s-averaged intensity both with, and without, correction (dechirping) for the leading effect of dispersion varying as $\sim \text{TEC}/f^2$. An example of these two versions of the intensity are shown in Figure A1. The solid curve is with dechirping, and the dashed curve is without. The data for this example are the same data as in the spectrogram of Figure 5(a). The most intense feature in the dashed curve, at $t=290 \mu\text{s}$, corresponds to the most intense feature in the solid curve, at $t=200 \mu\text{s}$. The time shift of the dashed curve is due to its lack of correction for ionospheric group delays. Because the TEC is known, so too is the optimal relative shift to align the features. The dashed curve is then shifted leftward by this optimal shift. The peak is identified as the peak of the *product of both curves after they are aligned*. This tends to exclude radar pulses, due to their random placement within the record, and to select for true lightning pulses. Given the frequently weak

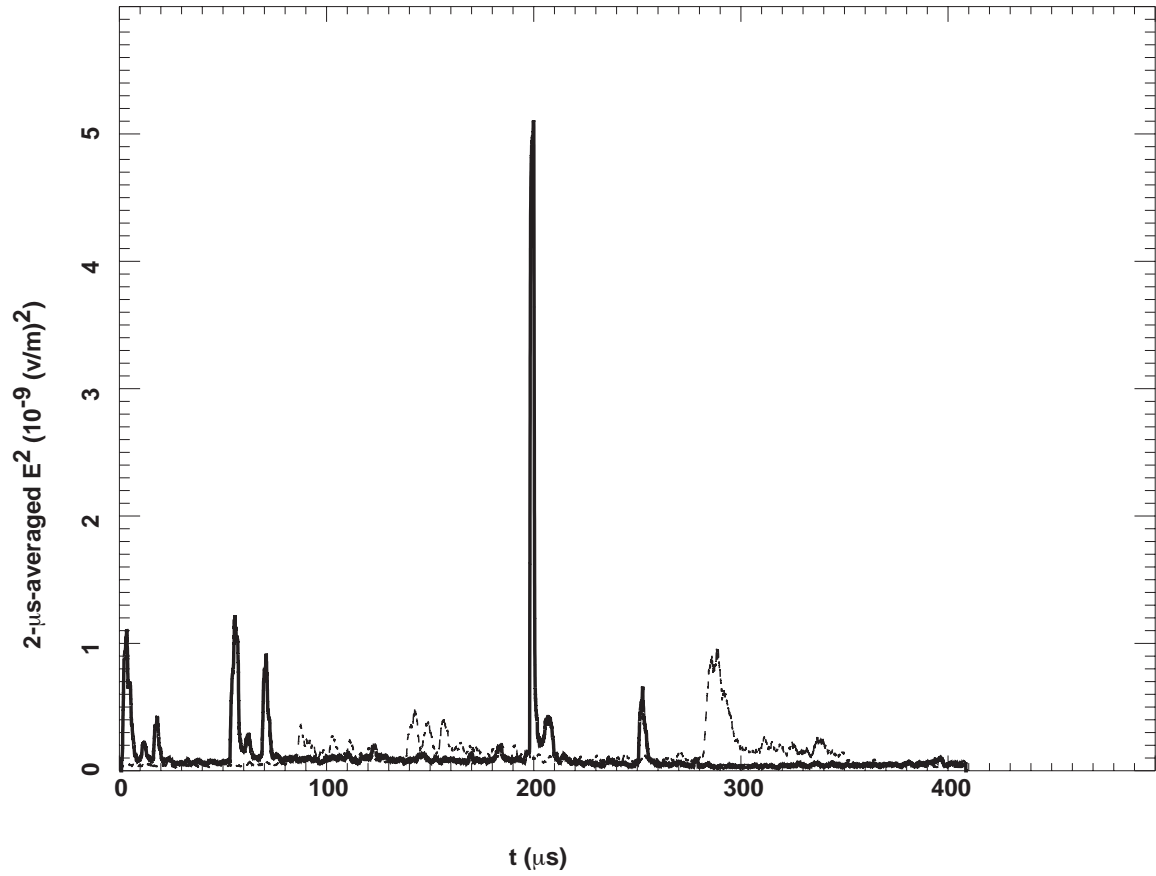


Figure A1: 2- μ s-averaged intensity versus time after suppression of carriers, for dechirped electric field (solid curve) and for original electric field (dashed curve). The data is the same from which is derived the spectrogram Figure 5(a) (see text).

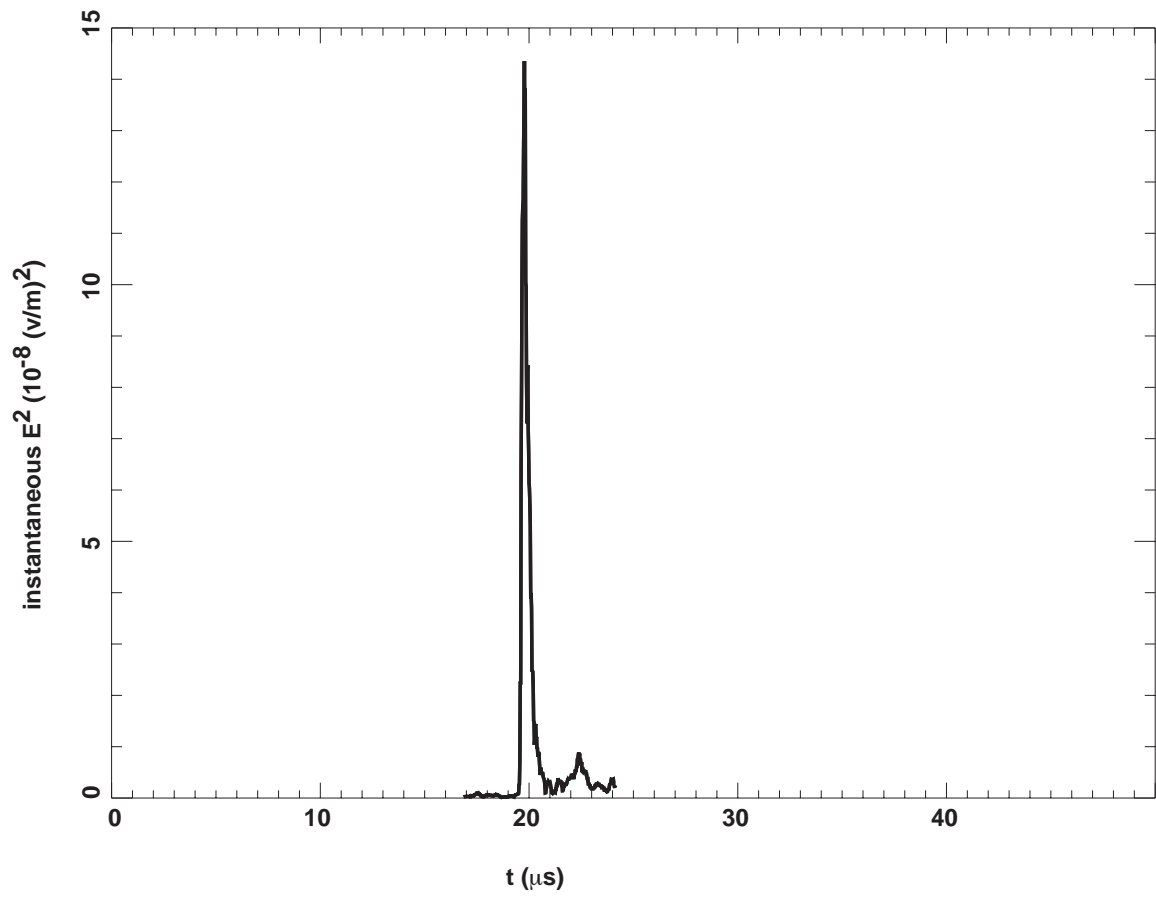


Figure A2: Detailed view of intensity versus time for the dechirped selected pulse from Figure A1, with the value suppressed to zero outside a $\sim 7\text{-}\mu\text{s}$ time window containing the pulse (see text).

intensity of the polarized/coherent pulses, this is an essential step to avoid selecting a radar signal as a “lightning pulse”.

Step 2: We wish also to compress that selected pulse, and remove all of the record outside of a narrow slice around the compressed pulse. Doing so will favor the pulse itself and disfavor noise that is more distributed in time. Having identified the true strongest pulse, we then select the peak and its immediate surroundings above a threshold (proportional to the selected peak) in the dechirped time-domain signal of E . The intensity for the selected pulse is shown in Figure A2; note that the selected segment of the dechirped signal is only $\sim 7 \mu\text{s}$ in duration in this case. The rest has been zeroed-out because it lies outside the first sub-threshold values. By first compressing the pulse (in the dechirping in Step 1) and then taking only a narrow slice of the data around the true peak, we have significantly excluded noise in the record. We take the time-domain electric field E of this dechirped, time-limited pulse, and re-chirp it by undoing the correction of dispersion. After this re-chirping, the E signal is shown in Figure A3. The width of this pulse is now $\sim 60 \mu\text{s}$, due to the dispersion that we have re-introduced. However, the noise in the re-chirped signal is only the noise deriving the narrow $7\text{-}\mu\text{s}$ segment shown earlier in Figure A2. In effect, the compression, followed by a narrow slice of selection, followed by de-compression of that slice, favors the broadband signal over the carrier noise by a factor of $\sim 60/7$. This is because the broadband lightning signal is truly compressed in the dechirping, while the modulated carriers (being narrow-band) are only shifted.

Step 3: The amplitude modulation, or beating, in the re-chirped pulse is evaluated by examining the 200-ns-averaged intensity (see Figure 3a above). The spectrum of the intensity (Figure 3b above) shows both the feature due to a modulation beat (at 1.45 MHz) and a level of random spectral noise evaluated in the regions (1) between the DC feature and the modulation feature, and (2) to the right of the modulation feature. The ratio of the modulation peak to the noise is the signal-to-noise ratio, or SNR, of the modulation peak. We also characterize the modulation peak by its spectral width; narrower is “better”. However, the spectral width cannot be smaller than the inverse of the dispersed signal duration for the pulse. That dispersed signal duration is due to the dispersive arrival times, and in the low band used here is $\sim (10 \mu\text{s}) \times (\text{TEC}/(10^{17} \text{ m}^{-2}))$ [Jacobson *et al.*, 1999]. Thus, the narrowest possible frequency width of the modulation peak is $(0.1 \text{ MHz})/(\text{TEC}/(10^{17} \text{ m}^{-2}))$. In the case of Figure 2 above, the TEC is $3.43 \times 10^{17} \text{ m}^{-2}$, so the narrowest width we may expect is $\sim 0.034 \text{ MHz}$. The observed width is only about 20% greater than this limit.

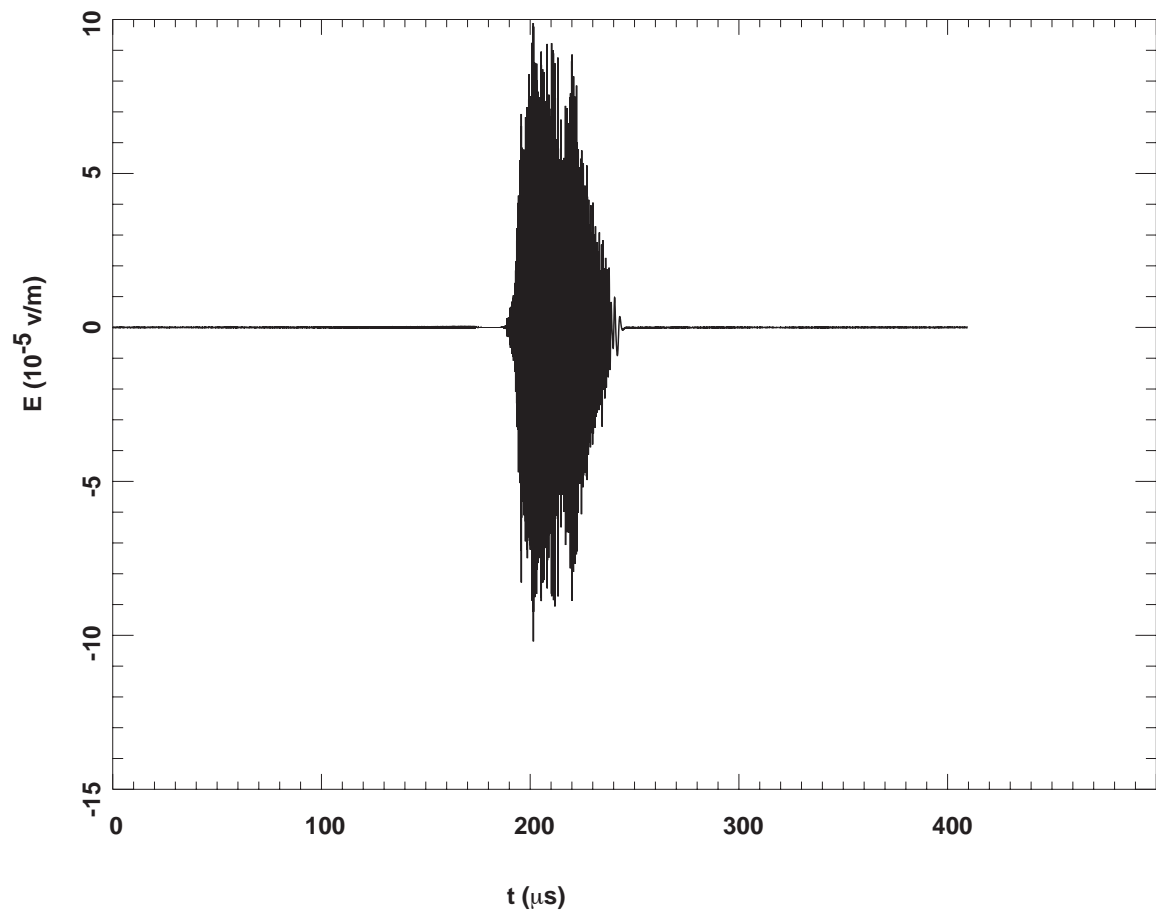


Figure A3: Detailed view of the re-chirped electric field waveform, for the limited pulse shown in Figure A1 (see text).

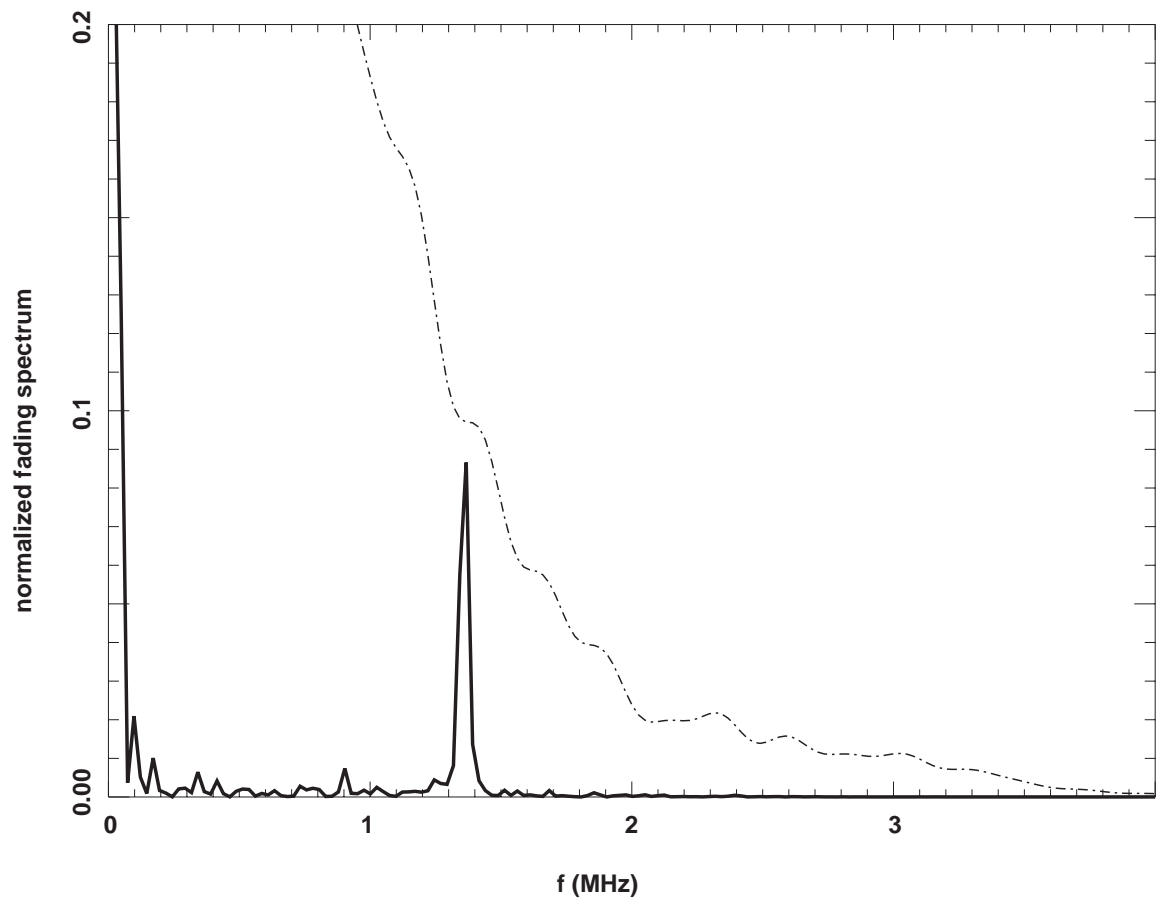


Figure A4: Amplitude-modulation spectra (similar to Figure 3b) for the rechirped data of Figure A3 (solid curve) and for the corresponding dechirped data (dashed curve).

Step 4: Finally, we perform an additional check to exclude modulated carriers. Just as we computed the spectrum of the modulation, and then both the SNR and the spectral width of the modulation peak, now we do the same for the peak in the dechirped E waveform. The true ionospheric amplitude-modulation effect should now be washed out by using the dechirped signal. However, if there were a narrow-band modulated carrier providing the amplitude modulation, then the modulation peak would be the same in both the dechirped and re-chirped cases. Figure A4 shows the comparison. The solid curve is the amplitude-modulation spectrum for the selected peak after being re-chirped (as shown earlier in Figure 3b). The dashed curve is the amplitude-modulation spectrum for the selected peak in its compressed state, without its being re-chirped. The peak in the solid curve is largely missing in the dashed curve. We quantify this by comparing the SNR of the solid curve, compared to the SNR of the dashed curve. The ratio of these is the “gain”. The higher the gain, the more certain it is that the amplitude modulation is due to polarization/coherence, as opposed to a modulated narrow-band carrier.

The thresholds for selecting polarized/coherent events (see Section 3 above) are as follows: The 15,346 polarized/coherent pulses (Figure 7b *et seq*) satisfy (1) $\text{SNR} > 20$, $\text{gain} > 10$, $\text{modulation frequency} > 0.3 \text{ MHz}$ and $\text{amplitude-modulation spectral width (MHz)} < 0.3/\text{TEC}$. The 90 exemplary polarized/coherent pulses chosen for manual analysis (Figure 6 above) have stricter thresholds: $\text{SNR} > 30$, $\text{gain} > 15$, $\text{modulation frequency} > 0.6 \text{ MHz}$, and $\text{amplitude-modulation spectral width (MHz)} < 0.2/\text{TEC}$.

A2. User-interactive analysis of low-band pulsewidth

As stated in the main article (Section 3), the method for determining low-band pulsewidth is used for the coherent/polarized pulses whose high-band signals are rarely strong enough to be useable. Figure 5(b) above shows the zoomed-in view of the selected pulse in the multi-pulse signal of Figure 5(a). The first-order dechirp has been applied to the signal’s ordinary mode (the left pulse). At this point, the user is prompted to indicate by hand, using the screen cursor, the approximate locus (frequency versus time) of the ordinary mode on the spectrogram. The algorithm then defines a zone extending $\pm 1 \mu\text{s}$ around the approximate locus and finds the power-weighted locus of time-versus-frequency within that zone. (The power is simply the spectrogram pixel values.) The residual variations in the ordinary-mode delay (as a function of frequency) are then fitted to a polynomial in frequency, and the fitted residual delays, plus the much larger-magnitude first-order delays, are then removed *from the original time-domain signal*. Figure A5(a) shows the resulting electric-field signal E, after this elaborate optimal dechirping for the ordinary mode. This signal is sampled at 50 samples per μs . Note that the extraordinary mode remains dispersed over several μs . Next, we repeat the optimal

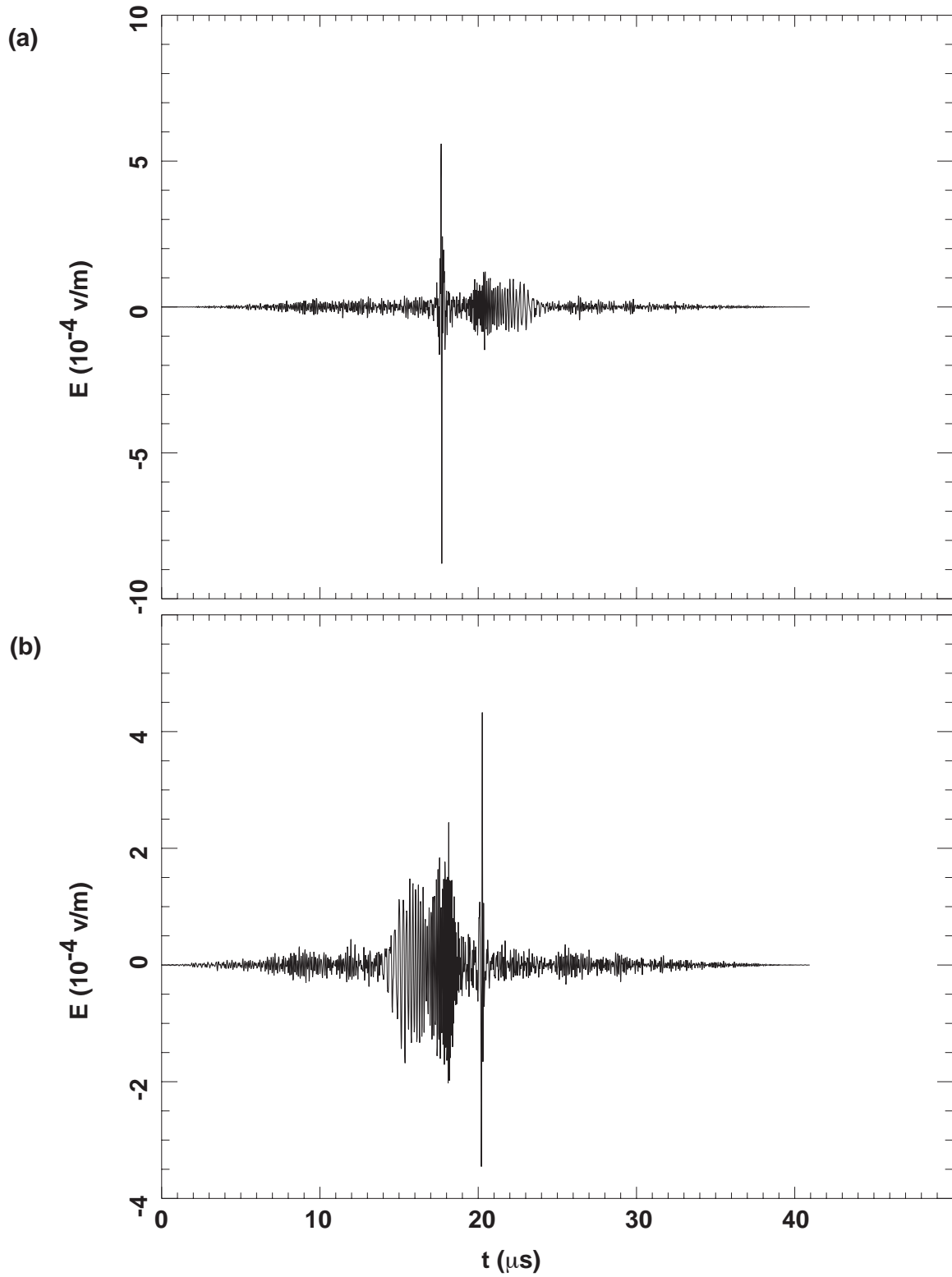


Figure A5: Electric field versus time, after optimally dechirping (a) for the ordinary mode and (b) for the extraordinary mode.

dechirp for the extraordinary mode. The optimally dechirped waveform in this case is shown in Figure A5(b). Note that the ordinary mode now remains dispersed over several μs , while the extraordinary mode is compressed.

Figure A6 shows the intensity E^2 versus time during $2.56 \mu\text{s}$ around (a) the ordinary mode peak and (b) the extraordinary mode peak. In each case the time-domain waveform has been optimally dechirped for the respective mode, prior to evaluation of the intensity.

To retrieve a pulsewidth from intensities such as shown in Figure A6, we compute the autocorrelation function (versus lag) of the intensity, separately for the ordinary and extraordinary modes, and find the width to $1/e$ of the central peak of the autocorrelation. The lesser of the two modes' widths is then used as the pulsewidth in Figure 6 (see Section 3 above.) This lengthy process is done for each of the 90 exemplary polarized, coherent pulses that are included in Figure 6.

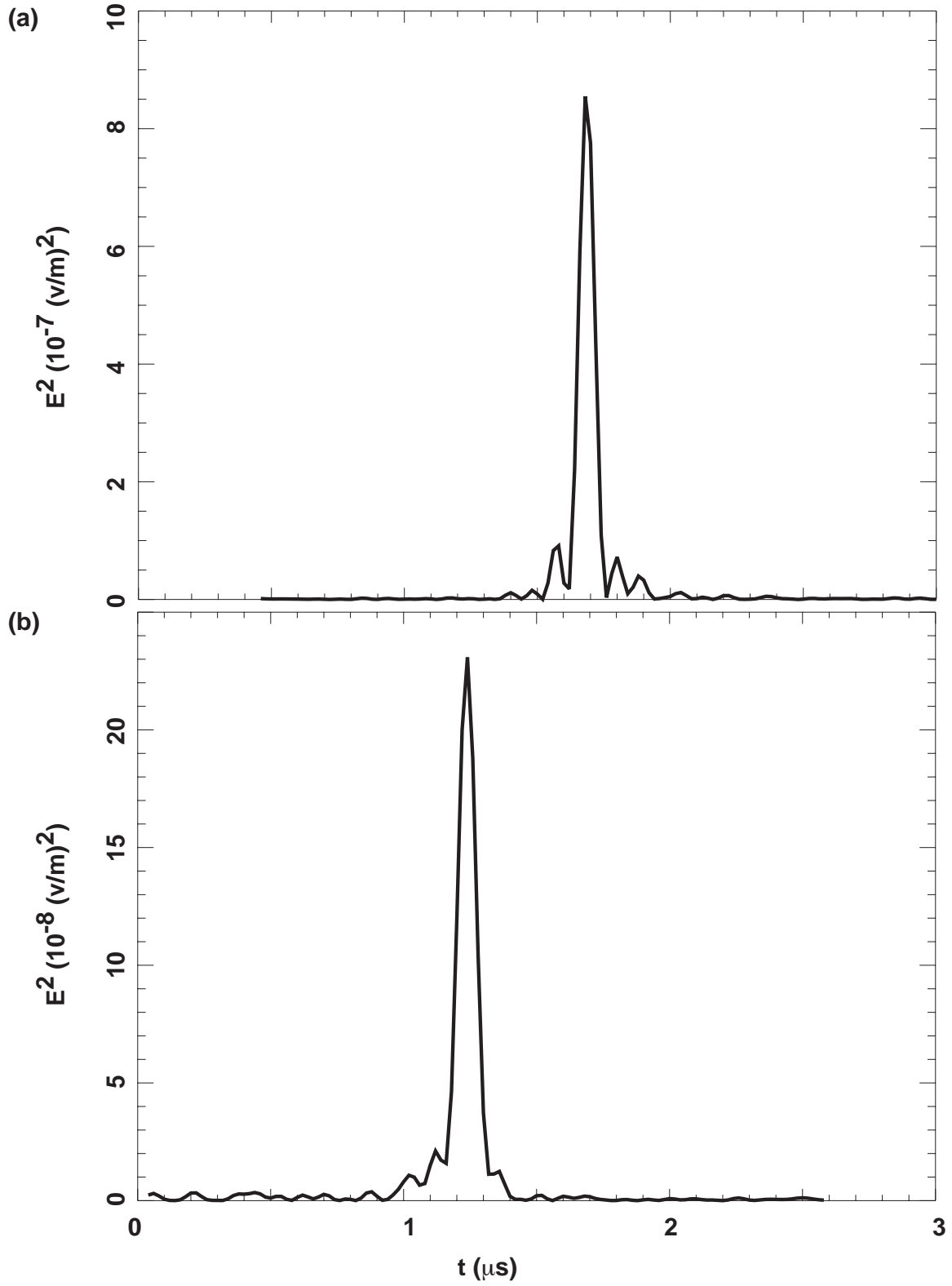


Figure A6: Intensity versus time, after optimally dechirping (a) for the ordinary mode and (b) for the extraordinary mode.

Acknowledgement

This work was performed under the auspices of the United States Department of Energy.

References

Boccippio, D.J., K. Driscoll, W. Koshak, R. Blakeslee, W. Boeck, D. Buechler, H. Christian, and S. Goodman, The Optical Transient Detector (OTD): Instrument characteristics and cross-sensor validation, *J. Atmos. Oceanic Tech.*, *17*, 441-458, 2000a.

Boccippio, D.J., S.J. Goodman, and S. Heckman, Regional differences in tropical lightning distributions, *J. Appl. Meteor.*, *39*, 2231-2248, 2000b.

Chang, D.-E., J.A. Weinman, C.A. Morales, and W.S. Olson, The effective of spaceborn microwave and ground-based continuous lightning measurements on forecasts of the 1998 Groundhog Day Storm, *Mon. Weather Rev.*, *129*, 1809-1833, 2001.

Christian, H.J., R.J. Blakeslee, S.J. Goodman, D.A. Mach, M.F. Stewart, D.E. Buechler, W.J. Koshak, J.M. Hall, W.L. Boeck, K.T. Driscoll, and D.J. Boccippio, The Lightning Imaging Sensor, in *11th International Conference on Atmospheric Electricity*, edited by H. Christian, NASA, Global Hydrology and Climate Center, NASA Marshall Space Flight Center, Huntsville, Alabama, 1999.

Cummins, K.L., M.J. Murphy, E.A. Bardo, W.L. Hiscox, R. Pyle, and A.E. Pifer, Combined TOA/MDF technology upgrade of U. S. National Lightning Detection Network, *J. Geophys. Res.*, *103* (D8), 9035-9044, 1998.

Holden, D.N., C.P. Munson, and J.C. Devenport, Satellite observations of transionospheric pulse pairs, *Geophys. Res. Lett.*, *22* (8), 889-892, 1995.

Jacobson, A.R., K.L. Cummins, M. Carter, P. Klingner, D. Roussel-Dupré, and S.O. Knox, FORTE radio-frequency observations of lightning strokes detected by the National Lightning Detection Network, *J. Geophys. Res.*, *105* (D12), 15,653, 2000.

Jacobson, A.R., S.O. Knox, R. Franz, and D.C. Enemark, FORTE observations of lightning radio-frequency signatures: Capabilities and basic results, *Radio Sci.*, *34* (2), 337-354, 1999.

Jacobson, A.R., and X.-M. Shao, Using geomagnetic birefringence to locate sources of impulsive, terrestrial VHF signals detected by satellites on orbit, *Radio Sci.*, 36 (4), 671-680, 2001.

Jacobson, A.R., and X.-M. Shao, FORTE satellite observations of very narrow radiofrequency pulses associated with the initiation of negative cloud-to-ground lightning strokes, *J. Geophys. Res.*, *in press*, 2002a.

Jacobson, A.R., and X.-M. Shao, On-orbit direction-finding of lightning radio-frequency emissions recorded by the FORTE satellite, *Radio Sci.*, *in press*, 2002b.

Kirkland, M.W., D.M. Suszcynsky, J.L.L. Guillen, and J.L. Green, Observations of terrestrial lightning at optical wavelengths by the the FORTE satellite photodiode detector, *J. Geophys. Res.*, 106 (D24), 33,499-33,509, 2001.

Krehbiel, P.R., An analysis of the electric field change produced by lightning, University of Manchester Institute of Science and Technology, Manchester, UK, 1981.

Krider, E.P., and C. Leteinturier, Submicrosecond fields radiated during the onset of first return strokes in cloud-to-ground lightning, *J. Geophys. Res.*, 101 (D1), 1589-1597, 1996.

Le Vine, D.M., Sources of the strongest RF radiation from lightning, *J. Geophys. Res.*, 85 (C7), 4091-4095, 1980.

Light, T.E., D.M. Suszcynsky, and A.R. Jacobson, Coincident Radio Frequency and Optical Emissions from Lightning, Observed with the FORTE Satellite, *J. Geophys. Res.*, 106 (D22), 28,223-28,231, 2001.

Light, T.E.L., and A.R. Jacobson, Characteristics of impulsive VHF lightning observed by the FORTE satellite, *J. Geophys. Res.*, *in press*, 2002.

Massey, R.S., and D.N. Holden, Phenomenology of transionospheric pulse pairs, *Radio Sci.*, 30 (5), 1645-1659, 1995.

Massey, R.S., D.N. Holden, and X.-M. Shao, Phenomenology of trans-ionospheric pulse pairs: Further observations, *Radio Sci.*, 33, 1755-1761, 1998a.

Massey, R.S., S.O. Knox, R.C. Franz, D.N. Holden, and C.T. Rhodes, Measurements of transionospheric radio propagation parameters using the FORTE satellite, *Radio Sci.*, 33 (6), 1739-1753, 1998b.

- Petersen, W.A., and S.A. Rutledge, On the relationship between cloud-to-ground lightning and convective rainfall, *J. Geophys. Res.*, 103 (D12), 14,025-14,040, 1998.
- Proctor, D.E., VHF radio pictures of cloud flashes, *J. Geophys. Res.*, 86 (C5), 4041-4071, 1981.
- Proctor, D.E., R. Uytendogaardt, and B.M. Meredith, VHF radio pictures of lightning flashes to ground, *J. Geophys. Res.*, 93 (D10), 12,683-12,727, 1988.
- Rhodes, C.T., X.M. Shao, P.R. Krehbiel, R.J. Thomas, and C.O. Hayenga, Observations of lightning phenomena using radio interferometry, *J. Geophys. Res.*, 99, 13059-13082, 1994.
- Rison, W., R.J. Thomas, P.R. Krehbiel, T. Hamlin, and J. Harlin, A GPS-based three-dimensional lightning mapping system: Initial observations in central New Mexico, *Geophys. Res. Lett.*, 26, 3573-3576, 1999.
- Roussel-Dupré, R.A., A.R. Jacobson, and L.A. Triplett, Analysis of FORTE data to extract ionospheric parameters, *Radio Sci.*, 36 (6), 1615-1630, 2001.
- Shao, X.-M., and A.R. Jacobson, Polarization observations of broadband VHF signals by the FORTE satellite, *Radio Sci.*, 36 (6), 1573-1589, 2001.
- Shao, X.-M., and A.R. Jacobson, Polarization observations of lightning-produced VHF emissions by the FORTE satellite, *J. Geophys. Res.*, *in press*, 2002.
- Shao, X.-M., C.T. Rhodes, and D.N. Holden, RF radiation observations of positive cloud-to-ground flashes, *J. Geophys. Res.*, 104 (D8), 9601-9608, 1999.
- Shao, X.M., and P.R. Krehbiel, The spatial and temporal development of intracloud lightning, *J. Geophys. Res.*, 101 (D21), 26,641-26,668, 1996.
- Shao, X.M., P.R. Krehbiel, R.J. Thomas, and W. Rison, Radio interferometric observations of cloud-to-ground lightning phenomena in Florida, *J. Geophys. Res.*, 100 (D2), 2,749-2,783, 1995.

- Smith, D.A., K.B. Eack, J. Harlin, M.J. Heavner, A.R. Jacobson, R.S. Massey, X.M. Shao, and K.C. Wiens, The Los Alamos Sferic Array: Ground Truth for the FORTE satellite, *J. Geophys. Res.*, *submitted*, 2001.
- Smith, D.A., X.M. Shao, D.N. Holden, C.T. Rhodes, M. Brook, P.R. Krehbiel, M. Stanley, W. Rison, and R.J. Thomas, A distinct class of isolated intracloud lightning discharges and their associated radio emissions, *J. Geophys. Res.*, *104* (D4), 4189-4212, 1999.
- Suszcynsky, D.M., M.W. Kirkland, A.R. Jacobson, R.C. Franz, S.O. Knox, J.L.L. Guillen, and J.L. Green, FORTE observations of simultaneous VHF and optical emissions from lightning: Basic Phenomenology, *J. Geophys. Res.*, *105* (D2), 2191-2201, 2000a.
- Suszcynsky, D.M., T.E. Light, S. Davis, M.W. Kirkland, J.L. Green, and J. Guillen, Coordinated Observations of Optical Lightning from Space using the FORTE Photodiode Detector and CCD Imager, *J. Geophys. Res.*, *106* (D16), 17,897-17,906, 2000b.
- Taylor, W.L., A VHF technique for space-time mapping of lightning discharge processes, *J. Geophys. Res.*, *83* (C7), 3575-3583, 1978.
- Taylor, W.L., E.A. Brandes, W.D. Rust, and D.R. MacGorman, Lightning activity and severe storm structure, *Geophys. Res. Lett.*, *11* (5), 545-548, 1984.
- Thomas, R.J., P.R. Krehbiel, W. Rison, T. Hamlin, J. Harlin, and D. Shown, Observations of VHF source powers radiated by lightning, *Geophys. Res. Lett.*, *28* (1), 143-146, 2001.
- Tierney, H., A.R. Jacobson, W.H. Beasley, and P.E. Argo, Determination of source thunderstorms for VHF emissions observed by the FORTE satellite, *Radio Sci.*, *36* (1), 79, 2001.
- Tierney, H.E., A.R. Jacobson, R. Roussel-Dupré, and W.H. Beasley, Transionospheric pulse pairs originating in marine, continental and coastal thunderstorms: Pulse energy ratios, *Radio Sci.*, *37*, 2002.
- Willett, J.C., J.C. Bailey, and E.P. Krider, A class of unusual lightning electric field waveforms with very strong high-frequency radiation, *J. Geophys. Res.*, *94* (D13), 16255-16267, 1989.

Willett, J.C., J.C. Bailey, C. Leteinturier, and E.P. Krider, Lightning electromagnetic radiation field spectra in the interval from 0.2 to 20 MHz, *J. Geophys. Res.*, *95* (D12), 20,367-20,387, 1990.

Willett, J.C., and E.P. Krider, Rise times of impulsive high-current processes in cloud-to-ground lightning, *IEEE Trans. Ant. Prop.*, *48* (9), 1442-1451, 2000.

Willett, J.C., E.P. Krider, and C. Leteinturier, Submicrosecond field variations during the onset of first return strokes in cloud-to-ground lightning, *J. Geophys. Res.*, *103* (D8), 9027-9034, 1998.

Williams, E.R., Chapter 13: The Electrification of Severe Storms, in *Severe Convective Storms*, edited by C.A.I. Doswell, American Meteorological Society, 2001.

Williams, E.R., M.E. Weber, and R.E. Orville, The relationship between lightning type and the convective state of thunderstorms, *J. Geophys. Res.*, *94*, 13213-13220, 1989.

Zipser, E.J., Deep cumulonimbus cloud systems in the tropics with and without lightning, *Mon. Weather Rev.*, *122* (8), 1837-1851, 1994.

Zipser, E.J., and K.R. Lutz, The vertical profile of radar reflectivity of convective cells: A strong indicator of storm intensity and lightning probability?, *Mon. Weath. Rev.*, *122* (8), 1751-1759, 1994.

Figure captions

Figure 1: Spectrograms of (a) strong intracloud pulse, and (b) polarized/coherent intracloud pulse. The ground echo is seen at a delay of $\sim 50 \mu\text{s}$ relative to the main pulse.

Figure 2: (a) Low-band intensity versus time for the strong pulse of Figure 1(a) above. Prior to evaluating the intensity $E^2(t)$, the carriers are suppressed, and the signal $E(t)$ is dechirped to first order. The echo is due to ground reflection. The “contrast” of the pulse is defined as the ratio of the peak to median intensity within the record. (b) Normalized autocorrelation function of the intensity shown in the top panel. The main peak’s halfwidth to $1/e$ furnishes a pulsewidth, and the signal-to-noise of the secondary peak furnishes a criterion (“snr”) for the ground-reflection echo’s readability.

Figure 3: Illustration of amplitude modulation for polarized/coherent pulse of Figure 1(b) above. (a) 200-ns-smoothed intensity (E^2) versus time, showing regular periodic amplitude modulation. (b) Spectrum of intensity. Secondary peak at $\sim 1.45 \text{ MHz}$ corresponds to the regular periodic amplitude modulation.

Figure 4: Illustration of amplitude modulation for strong pulse of Figure 1(a) above. (a) 200-ns-smoothed intensity (E^2) versus time, showing irregular amplitude modulation due to random fading. (b) Spectrum of intensity. There is no distinct or unique secondary peak in this case.

Figure 5: Spectrograms of polarized/coherent intracloud pulse shown earlier in Figure 1(b). (a) Entire 400- μs record, with 1.3- μs time resolution. The main pulse lies between the two vertical, dashed lines. (b) Detail of main pulse (from $t \sim 300 \mu\text{s}$ in (a)), after first-order dechirping for ordinary mode, with 0.6- μs time resolution. The 40- μs time range is centered on the main pulse.

Figure 6: Normalized histograms of intensity autocorrelation function $1/e$ halfwidth, for all 9034 strong pulses (solid curve, using high-band) and for the 90 exemplary polarized/coherent pulses (dashed curve, using low-band).

Figure 7: Observed probability of there being a same-flash neighbor per 0.01-s separation bin. The neighbor candidate pool comprises all FORTE VHF events having a low-band channel and having a well-determined TEC, without requiring either strong or polarized/coherent pulses (see text). (a) The key-event pool is the overall pool also used

as neighbor events. (b) The key-event pool is restricted to the 15,346 polarized/coherent events (see text). (c) The key-event is restricted to the 17,243 strong events (see text).

Figure 8: Histogram of the total number of neighbors per strong-pulse key event within 0.0 to 0.6 s after key event. The key events are restricted to those strong IC pulses having neighbors in the following 0.6 s but no neighbors in the preceding 2.0 s.

Figure 9: Cumulative probability of neighbor-to-key low-band peak-power ratio, for neighbors within 0.0 to 0.6 s after key event (solid curve) and for neighbors within 2.0 to 10.0 s after key event (dashed curve). The key events are restricted to those strong IC pulses having neighbors in the following 0.6 s but no neighbors in the preceding 2.0 s.

Figure 10: Development of an intracloud flash initiated by a strong IC pulse. (a) Pulse-pair separation (proportional to emission height) versus time. (b) Low-band peak intensity versus time. The symbol size is proportional to intensity.

Figure 11: Overlay of 14 successive strong-pulse intensities versus time, with a logarithmic vertical scale.

Figure 12: Los Alamos Sferic Waveform Array vertical electric field data examples for (a) a Narrow Positive Bipolar Event (NPBE), (b) a Narrow Negative Bipolar Event (NNBE), and (c) an ordinary sferic.

Figure 13: Histograms of {sferic -origination time} minus {FORTE VHF signal-origination time}, for (a) 1943 ordinary sferics, and (b) 496 Narrow Bipolar Events.

Figure A1: 2- μ s-averaged intensity versus time after suppression of carriers, for dechirped electric field (solid curve) and for original electric field (dashed curve). The data is the same from which is derived the spectrogram Figure 5(a) (see text).

Figure A2: Detailed view of intensity versus time for the dechirped selected pulse from Figure A1, with the value suppressed to zero outside a ~ 7 - μ s time window containing the pulse (see text).

Figure A3: Detailed view of the re-chirped electric field waveform, for the limited pulse shown in Figure A1 (see text).

Figure A4: Amplitude-modulation spectra (similar to Figure 3b) for the re-chirped data of Figure A3 (solid curve) and for the corresponding dechirped data (dashed curve).

Figure A5: Electric field versus time, after optimally dechirping (a) for the ordinary mode and (b) for the extraordinary mode.

Figure A6: Intensity versus time, after optimally dechirping (a) for the ordinary mode and (b) for the extraordinary mode.